The Impacts of Stratification on High Latitude Ocean Mixing: a case study of internal waves in Storfjorden, Svalbard

Tamara Beitzel Barriquand, Pascale Bouruet-Aubertot, Yannis Cuypers, Frédéric Vivier, Antonio Lourenço, Hervé Le Goff

To cite this version:

Tamara Beitzel Barriquand, Pascale Bouruet-Aubertot, Yannis Cuypers, Frédéric Vivier, Antonio Lourenço, et al.. The Impacts of Stratification on High Latitude Ocean Mixing: a case study of internal waves in Storfjorden, Svalbard. Continental Shelf Research, 2015, 110, pp.162-182. 10.1016/j.csr.2015.10.001 . hal-01220406

HAL Id: hal-01220406
https://hal.sorbonne-universite.fr/hal-01220406v1

Submitted on 26 Oct 2015

The Impacts of Stratification on High Latitude Ocean Mixing: a case study of internal waves in Storfjorden, Svalbard

Tamara Beitzel Barriquand[a,*], Pascale Bouruet-Aubertot[a], Yannis Cuypers[a], Frédéric Vivier[a], Antonio Lourenço[a], Hervé Le Goff[a]

[a]*Laboratoire d'Océanographie et du Climat: Expérimentaions et Approches Numériques, Institut Pierre Simon Laplace (LOCEAN-IPSL), Sorbonnes Universités, UPMC Univ. Paris 06, Paris, France.*

Abstract

Hydrographic and velocity measurements were taken over four different time periods from April and May 2005-2007 at adjacent stations in Storfjorden, Svalbard. Different environmental conditions, including winds, ice cover, and water mass contributions, yield notably different stratification (N^2) profiles among the time series. When classified according to the Gerkema (2001) classification system, the stratification profiles span the spectrum with two profiles resembling that of a two-layer fluid, one resembling more closely a fluid of constant stratification, and one falling in between the two extremes. The different N^2 profiles elicit sharply contrasting modal responses from the internal wave field, which is dominated by mode 1 during the two time series most resembling a two-layer fluid, and nearly evenly spread out among the first five modes during the time series with a nearly constant stratification. Turbulent dissipation rates determined from fine-scale parameterizations reveal an average rate on the order of $10^{-9} W kg^{-1}$ for all time series with an associated average diapycnal diffusivity of $10^{-5} m^2 s^{-1}$ - $10^{-4} m^2 s^{-1}$. Turbulent heat fluxes, determined from the estimated turbulent dissipation rates, ϵ, were found to have a relative maximum at the tops of the pycnoclines, with values up to $1 W m^{-2}$, typical of ice-covered conditions. The turbulent

---

[*]Corresponding Author. LOCEAN, UPMC, BP 100, 4 place Jussieu 75252 Paris Cedex 05 France. US Tel.: +1 805.796.1999, French Tel.:+33 (0)6.77.62.04.57

Email address: `tamara.tpr@gmail.com, tblod@locean-ipsl.upmc.fr` (Tamara Beitzel Barriquand)

Preprint submitted to Continental Shelf Research *October 12, 2015*

dissipation rate and diapycnal diffusivities for each time series vary with the Gerkema (2001) stratification profile rankings, and are elevated for the time series most resembling a fluid of constant stratification, and reduced for the time series most similar to a two-layer fluid.

Keywords: Internal Waves, Stratification, Mixing, Turbulence, Arctic, Storfjorden

---

1. Introduction

High latitude internal waves have distinct properties due to their geolocation. Ice cover reduces the wind forcing that generates most of the inertial waves in lower latitudes. This decreased surface forcing, coupled with increased dissipation due to the turbulent boundary layer beneath the rough ice, leads to significantly lower internal wave energy in the Arctic, as compared to lower latitudes (Levine et al., 1985; Levine, 1990). Even with the recent decline in sea ice, internal wave energy in the Arctic has remained low over the past 30 years (Guthrie et al., 2013). Guthrie et al. (2013) attribute this continued low internal wave energy to enhanced boundary layer dissipation due to increased stratification, and thus increased internal wave horizontal velocity above the pycnocline, relative to the rest of the water column.

Another peculiarity of high latitudes is that the diurnal as well as certain components of the semidiurnal, including M_2, tidal frequencies are subinertial, so the baroclinic waves generated by these tidal components are evanescent. While in areas of weak stratification the nontraditional β terms, which come into play in the full projection of the Coriolis force, may expand the range of internal wave frequencies, allowing near-inertial waves to propagate beyond their inertial latitude, (Gerkema & Shrira, 2005a,b) and allowing energy to be focused within these waveguides (Winters et al., 2011), the internal tide remains largely evanescent above the inertial latitude. Previous work suggests that a significant part of the baroclinic tidal energy is dissipated by the instability of these evanescent waves, as energy is transferred to short topography-scale nonlinear internal waves (Vlasenko et al., 2003).

Along with the dissipation due to these unstable evanescent waves, other processes particular to high latitudes, including deep water formation, can impact the energy budget. Deep water formation takes place at high latitudes in openings in the ice known as polynyas, where heat transfers rapidly from the relatively warmer ocean to the colder atmosphere (Schauer, 1995). As the heat is lost to the atmosphere, the sea water freezes, rejecting its saline content in the process, and forming new dense waters which then sink rapidly, destabilizing the water column, and increasing turbulent mixing (Skogseth et al., 2013). Since dissipation at high latitudes is due to multiple processes, the rate of turbulent dissipation varies greatly, ranging from 10^{-10} to $10^{-6} Wkg^{-1}$ due to background mixing and breaking internal waves (Fer et al., 2010; Sundfjord et al., 2007), to up to $10^{-5} Wkg^{-1}$ during deep water formation (Jardon et al., 2011).

These deep water formation events not only incite instantaneous mixing, but also rapidly alter the shape of the stratification profile. The goal of this study is to look at how these highly variable stratification profiles impact the dynamics and dissipation of the internal wave field at high latitudes. If we can determine what factors control internal wave dynamics and dissipation under these conditions, we can get a better picture of how the ocean mixes at high latitudes.

In order to get some insight into what controls the dynamics and dissipation of high-latitude internal waves, we look at high-latitude data from multiple campaigns in Storfjorden, a fjord in the Svalbard Archipelago. As can be seen in Figure 1, Storfjorden, encircled by three islands and a large sill at a depth of $120m$, is semi-enclosed with only two narrow gateways to the northeast (Skogseth et al., 2005; Quadfasel et al., 1988). This Arctic fjord is a highly productive site of deep water formation, responsible for nearly 5-10% of all Arctic Deep Water (Quadfasel et al., 1988). Deep water formation takes place inside the fjord in a recurring polynya that opens during northeasterly winds in winter, allowing heat transfer to the atmosphere, and subsequent ice production and brine release (Skogseth et al., 2013). While the average stratification in Storfjorden is always relatively weak, with typical average N^2 values never exceeding approximately $10^{-4}s^{-1}$, the vertical structure of the stratification profiles can change rapidly, in just a few days, due to these brine release events, or the intrusion of Atlantic water masses (Skogseth et al., 2005). The impact of these strong and rapid modifications of the stratification profiles on the dynamics and dissipation of high-latitude internal waves has never been quantified.

According to Skogseth et al. (2013), the processes occurring in Storfjorden are representative of those in the Arctic shelf seas, which makes this semi-enclosed basin a natural laboratory for studying high-latitude internal wave dynamics and the resultant turbulent mixing. A previous study in Storfjorden, Jardon et al. (2011, 2014) analyzed ice-tethered moorings drifting southward from the northwestern part of the fjord for a 10-day period in late March 2007. Jardon et al. (2011) found turbulent eddy diffusivities ranging from $10^{-4} - 10^{-6} m^2/s$, which they attributed to breaking internal waves. This paper builds upon Jardon et al. (2011, 2014), by analyzing hydrographic and velocity data from three subsequent years, at a fixed location, to get a deeper understanding of how interannual variations in Storfjorden, specifically changes in the stratification profile, impact internal wave dynamics and dissipation.

An overview of the measurement locations, instrumentation, and data collection methods are laid out in Section 2. The hydrographic data, including water masses and stratification, are presented in Section 3.1. The currents are presented and discussed in Section 3.3. In Section 4, the internal waves are characterized, including the energetics of their various frequency components, their associated power spectra, and vertical modes. Finally, the amount of energy dissipating locally is determined by analyzing several different turbulent mixing parameterizations, their associated diapycnal diffusivities, and the resultant heat flux (Section 5).

2. Data

2.1. CTD and ADCP data

The data come from Conductivity/Temperature/Depth (CTD) and Acoustic Doppler Current Profiler (ADCP) measurements obtained during several campaigns in Svalbard aboard the Polar Yacht Vagabond, wintering in Storfjorden. The campaigns include the BRINES campaign, which consisted of three field experiments in April 2005, April 2006, and May 2006, as well as the ICE-DYN campaign of April 2007. The data were collected through the ice at three different nearly co-located stations on the western side of Storfjorden, Svalbard. The stations were located between $18.53^o E - 18.65^o E$, and $77.86^o N - 77.91^o N$, as can be seen in Figure 1.

CTD casts were taken by a Seabird SBE 19 plus CTD which was lowered through the ice from a hand-cranked winch on a sledge, at an interval of approximately 30 minutes, during the BRINES campaign from 28-29 April 2005, 8-9 April 2006, and 2-3 May 2006, as well as during the ICE-DYN experiment from 27-28 April 2007. The data were later binned into 1-meter bins.

At the latitude of our stations, the inertial frequency is $1.426 \times 10^{-4}s^{-1}$, with a period of 12.24 hours, which falls in between the S_2 and M_2 semidiurnal tidal frequencies. So, at the resolution of our measurements, inertial waves at our stations are almost indistinguishable from the internal semidiurnal tide. In order to measure the contributions from these important frequencies, the CTD casts were performed to encompass at least one inertial/semidiurnal period. The longest of the four CTD time series, April 2005, spans about two semidiurnal tidal cycles, or nearly two inertial wave periods. The three shorter CTD data sets from April and May 2006, and April 2007 each span approximately one semidiurnal/inertial cycle.

ADCP measurements were taken with an ice-tethered downward-looking Teledyne RDI broadband 300 kHz ADCP approximately every five minutes with a 4-meter resolution during all four time series. The longest ADCP time series, April 2006, spans more than six inertial, or semidiurnal, periods. The second-longest, April 2005, spans just over two periods, and May 2006 spans just over one period. Due to a battery failure during April 2007 which caused the ADCP to stop working before the CTD profile could be acquired, the April 2007 ADCP time series is just under half an inertial period. The relative length of the different time series can be seen in Figure 1.

2.2. Environmental Data

The environmental conditions affecting our data, including winds and ice cover, were obtained by examining ancillary data coincident with our measurements.

Ice Cover

The relative importance of the ice cover during the four different time series is found by examining high-resolution ice charts from the Norwegian Meteorological Institute. The ice charts are based on satellite imagery, including 1.5-km resolution Synthetic Aperture Radar data from the satellites Radarsat and Envisat, 10-km resolution Ocean and Sea Ice Satellite Application Facility (O&SI SAF) data derived from Defense Meteorological Satellite Program Special Sensor Microwave Imager (DMSP SSM/I) satellite data, 7-km resolution QuickScat Seawinds derived ice edge, as well as observations from ships and aircraft (PolarView, 2012).

Winds

Since there is no satellite cover of winds at latitudes as far north as our CTD/ADCP stations, we have looked at both the NCEP/NCAR and ECMWF reanalysis wind data. The reanalysis data nearest to our stations is located at 77.14° N, 18.75° E. While these wind data may not give an exact wind stress at the measurement sites, they do reveal the relative strength of the winds during the different time series. The mean NCAR/NCEP reanalysis wind vectors range from 0.69 m/s during April 2005, to 2.6 m/s during May 2006, to 4.3 m/s during April 2007, up to 7.1 m/s during April 2006 (Kalnay, 1996). ECMWF reanalysis wind data are similar in magnitude and direction, ranging from 0.71 m/s in April 2005 to 6.2 m/s in April 2006 (ECMWF, 2014).

3. Hydrography and Currents

3.1. Water Masses

According to the literature, the main water masses contributing to the waters in Storfjorden include Arctic Water (ArW), which enters the fjord from the east via the East Spitsbergen Current, and Atlantic Water (AW), carried into the fjord from the south by the Norwegian Atlantic Current, both of which circulate cyclonically through the fjord. In addition to these two water masses formed outside the fjord, local brine rejection leads to the formation of Brine-enriched Shelf Water (BSW) in the fjord. Brine rejection primarily occurs in ArW in the northeastern section of the fjord (Loeng, 1991; Schauer, 1995; Skogseth et al., 2005).

To determine which water masses contribute to the water columns observed during the four time series, we plot the data from each time series on a potential temperature-salinity ($\Theta - S$) diagram (Figure 2). All or part of each observed water column share similar water characteristics with BSW, with $S > 34.8$ and $T < -1.5^oC$, based on the water mass classification from Loeng (1991) and Skogseth et al. (2005).

While the deeper waters in April 2005 share properties of BSW just like the other three time series, the waters in the top approximately $40m$ share characteristics with the less-dense Arctic Water (ArW), which is not present in any of the other three time series. It is interesting to note that while we did not observe any ArW at our CTD station in April 2007, Jardon et al. (2014) observed ArW further south in Storfjorden just one month prior to our observations.

3.2. Stratification

The stratification, as defined by the square of the Brunt-Vaisala, or buoyancy, frequency, $N^2 = -g/\rho_0 \frac{d\rho}{dz}$, was calculated for each time series, and the time-mean vertical profiles are shown in Figure 3. Even though each CTD time series was obtained in similar locations during similar times of year (April and May), each time period is distinguished by a remarkably different N^2 profile, as seen in Figure 3. The N^2 profile from April 2005 (Figure 3a) shows a marked change in density, a strong pycnocline, at approximately $40m$ depth, the depth at which the water properties shift from those of ArW to those of BSW (Figure 2). While the April 2007 N^2 profile also reveals a strong pycnocline in the top of the water column, around $20m$ depth, this strong pycnocline is not unique, but rather is followed by another somewhat less strong pycnocline deeper in the water column (Figure 3b). Similarly, the May 2006 N^2 profile (Figure 3d) consists of several weaker pycnoclines throughout the water column, and April 2006 (Figure 3c) has almost no distinct pycnocline, but rather a nearly constant stratification throughout the water column.

While the April 2006 N^2 profile looks markedly different from that of April 2005, both of these seemingly incongruous stratification profiles show almost no stratification in the top of the water column to about $20m$ depth, revealing the presence of a mixed layer during these two time periods. From our stratification profiles (Figure 3 a and c), we can see that the water begins to become stratified at about $23m$ for April 2005 and about $14m$ for April 2006. These depths correspond to a change in density of $.01kg/m^3$ from the surface, consistent with the criterion used by Fer & Drinkwater (2014) to define the mixed layer depth in the Barents Sea. We take this to be the depth of our mixed layer during these two time series. In contrast, the N^2 from the two other time series, May 2006 and April 2007 (Figure 3d and b), do not have clearly defined mixed layers, but rather a changing stratification all the way to the surface. This difference in mixed layer depth (MLD) corresponds to differences in relative ice cover, as can be seen in Figure 4. The ice cover in Storfjorden during the time series range from ”close drift ice” (70-90% cover) in April 2006, to ”very close drift ice” (90-100% cover) in April 2005, and ”fast ice” (100% cover) in May 2006 and April 2007. There is less ice cover during the two periods with a mixed layer, April 2005 and April 2006,(Figure 4a and c), than during the other two periods where the observed stratification extends to the surface, May 2006 and April 2007 (Figure 4b and d).

To objectively compare the N^2 profiles, we have fit each profile to a simple theoretical stratification profile from Gerkema (2001), who used a simple stratification model to analyze the effect of the thermocline on the vertical mode diffraction of an internal tidal beam. While our data are not dominated by an internal tidal beam, but rather span the spectrum of the internal wave field, we are similarly interested in which vertical mode is favored by which stratification profile, and so are also interested in objectively comparing the stratification profiles. The Gerkema (2001) 2c-layer model, based on the stratification classification system first proposed by Baines (1982), consists of a mixed upper layer, a constantly stratified lower layer (from which the "c" is derived), and a jump in density across the interface between the layers (the pycnocline). Based on this simple stratification model, Gerkema (2001) defines the objective parameter $\gamma = \frac{(g'd)^{1/2}}{N_c H}$, where g' is the reduced gravity (g times the relative difference in density across the pycnocline), d is the depth of the pycnocline, N_c is the constant stratification of the lower layer, and H is the total water depth, which is a finite constant. Since the numerator of γ is the phase speed of a wave in a two-layer system, and its denominator, that of a wave in a fluid of constant stratification, γ indicates whether the stratification is more similar to that of a uniformly-stratified fluid ($\gamma = 0$), or that of a two-layer fluid ($\gamma = 1$).

Our N^2 profiles are more complex than those in Gerkema (2001), however, so we cannot simply fit them to the 2c-layer model. Since there is no clearly defined interface, but rather a more gradual change in density between the top and bottom of the water column, following Mercier et al. (2012), we first looked at the density profiles to identify the points of inflection which define the top and bottom of each pycnocline, z_t and z_b, respectively. We can then calculate $\gamma^2 = \int_{z_b}^{z_t} (\frac{z}{H^2})(\frac{N^2}{N_c^2}) dz$, where $H = 80m$, the approximate water depth at our stations (see Figure 1), and N_c is the average stratification below the pycnocline. As can be seen from this formulation, γ depends on two factors: the ratio of the thickness of the pycnocline (z_t and z_b) relative to depth H and the ratio of stratification in the pycnocline (N^2) to that in the region below (N_c^2).

We can then compare the dimensionless parameter γ for each of our N^2 profiles. For the two profiles with strong pycnoclines in the top of the water column, April 2005 and April 2007, γ is 0.62 and 0.65 respectively (Figure 3a and b). This value compares favorably with the value for the regime with a very strong thermocline in Gerkema (2001), with a γ of 0.61. Note that γ characterizes only the upper $40m$ in April 2007, and does not take into account the second pycnocline deeper in the water column. The profile with the weakest pycnocline, April 2006, has a γ equal to 0.16 (Figure 3c), which compares favorably with the moderate thermocline regime in Gerkema (2001), with a γ of 0.12. The profile with multiple moderately strong pycnoclines, May 2006, has a γ of intermediate strength, with a value of 0.32 (Figure 3d).

Based on the γ's we calculated, we expect the April 2005 and April 2007 internal waves to behave more like those of a two-layer fluid, those of April 2006 to behave more like waves in a fluid of constant stratification, and those of May 2006 to behave somewhere in between these two regimes.

3.3. Currents

An overview of the space-time structure of the velocity field at each station is presented in Figures 5 - 8, starting with the barotropic (depth-mean velocity) signal represented in Figure 5. As can be seen in Figure 5a and d, both the zonal and meridional barotropic velocities during April 2005 and April 2006 reveal a semidiurnal/inertial barotropic signal. These two time series also reveal both a lower frequency modulation, as well as higher-frequency signals at ~ 4 and ~ 6 hours.

The average value of the barotropic current indicates a southwesterly flow at nearly all stations. This southwesterly flow is consistent with the cyclonic circulation that has been well-documented in Storfjorden (Loeng, 1991; Schauer, 1995). The magnitude of the average barotropic current is on the order of $5 - 10$ cm/s. For comparison, we ran the Arctic Ocean Tidal Inverse Model (AOTIM-5) (Padman & Erofeeva, 2004), which also yields an average barotropic current of a few cm/s for all stations.

The baroclinic velocity, $\mathbf{U}_{bc}$, the total velocity minus the barotropic velocity, is represented in Figure 6. The magnitude of the baroclinic velocities is of the same order as that of the barotropic velocities. All of the baroclinic time series reveal opposite directions in the top and bottom of the water column, indicating a mode-1 response, in the zonal direction (top of Figure 6). This mode-1 response is even more pronounced in the meridional direction (bottom of Figure 6). While this pattern is present in all the time series, it is much less apparent in April 2006, the time series with the weakest stratification (see Figure 3c), which instead reveals significant vertical propagation of internal waves in both the zonal direction, in particular on 7 April 2006 from 06:00 to 18:00 (Figure 6d), as well as in the meridional direction (Figure 6h).

Taking the time mean of the baroclinic velocities over a discrete number of inertial periods (which at this latitude is basically a discrete number of semidiurnal tidal periods), reveals significant time-mean baroclinic currents (Figure 7). The time-mean currents in April 2005 and April 2007 vary in direction from northeast at the surface to southwest at depth.

4. Internal Waves

4.1. Baroclinic Perturbation Velocity

To isolate the internal wave field, the time-mean baroclinic currents must be subtracted from the baroclinic velocity ($\mathbf{U}_{bc}$) field, ideally without subtracting any contribution from the underlying internal wave field. Since the main contribution to the internal wave field comes from near-inertial and semidiurnal frequencies and their harmonics, subtracting whole number multiples of the semidiurnal/inertial time period will not diminish these signals. We have defined the baroclinic perturbation velocities, $\mathbf{U}'_{bc}$, as the difference between $\mathbf{U}_{bc}$ and the time-mean baroclinic current. It is important to note, however, that since the April 2007 time series spans half of one semidiurnal period, when the time-mean current is subtracted from this time series, some of the semidiurnal/inertial energy is unavoidably lost. $\mathbf{U}'_{bc}$ for all stations can be seen in Figure 8.

After the time-mean baroclinic currents have been subtracted, the mode-1 response is no longer dominant, but rather the velocities change direction at multiple points in the water column, indicating the presence of other higher modes (Figure 8). The absence of the dominant mode-1 signal allows the vertical propagation of the internal waves to be clearly seen in all time series, for example between 28 April 2005 at 18:00 and 29 April 2005 at 06:00 in Figure 8e. Despite the similarities in vertical structure, however, significant discrepancies in the magnitude of the velocity fields exist. The two time periods with the greatest γ values, April 2005 and April 2007, have the smallest average perturbation velocities, on the order of $.01 m/s$, as compared to $.016 m/s$ during the period with an intermediate γ value, May 2006, and $.02 m/s$ during the period with the smallest γ value, April 2006. This energetic time series is less dominated by the semidiurnal/inertial period, and appears to have contributions from other higher-frequency signals of approximately 3 and 6 hours.

4.2. Energetics

In order to characterize the internal wave field and how it contributes to the energy budget, we calculate its mechanical energy, both that due to its isopycnal displacement (potential energy) and that due to its velocity (kinetic energy). Since the perturbation velocity time series (Figure 8) reveal semidiurnal/inertial signals, as well as 3- and 6-hour signals, the contribution from each of these specific signals is analyzed. The modal response of each of these components is then determined, along with the contribution of each of the vertical modes to the overall internal wave energetics.

4.2.1. Mechanical Energy

The available potential energy (APE) of the internal wave field is $\frac{1}{2}\eta^2 N^2$, where η, the isopycnal displacement, is $\rho'/\frac{d\rho}{dz}$, and ρ' is the perturbation from the time-mean density at each depth. The kinetic energy (KE) of the internal wave field is $KE = 1/2(\mathbf{u}^2 + \mathbf{v}^2)$. The KE was calculated for the baroclinic velocities (KE_{bc}), as well as the baroclinic perturbation velocities (KE'_{bc}).

In order to calculate the component of the kinetic and potential energies due to the semidiurnal internal tide, and that due to the 3- and 6-hour signals, the velocities and the isopycnal displacements must be isolated at those specific frequencies. Since the time series are not long enough to distinguish specific components, we have separated the various components using a harmonic analysis, following the method laid out in Gerkema & van Haren (2007), who separated the various components by assuming that different components are orthogonal, mimicking a Fourier transform. Since this method does not allow us to distinguish between nearby frequencies, we have lumped nearby frequencies together around each of the signals of interest before performing the frequency transformation. For example, M_2, S_2, and the inertial frequency were all grouped together as one frequency, and will henceforth be referred to as the semidiurnal (sd) frequency.

For all time series, the semidiurnal component of both the potential and kinetic energies is the biggest contributor to the energy of the internal wave field, followed by the 6-hour component, and then the 3-hour component. The time mean of the various components of the KE are plotted in Figure 9.

Figure 9 reveals a node, an energy minimum, in the baroclinic velocities (KE_{bc}) in the middle of the water column in April 2005 and April 2007, indicative of a mode-1 response during these two time series. May 2006 similarly shows a local node in the top of the water column, as well as a second local node in the bottom, but this nodal pattern is entirely absent from the

KE_{bc} in April 2006. Once the time-mean currents have been subtracted, and just the KE'_{bc} remains, this strong nodal feature disappears, and is not distinguishable in the semidiurnal, KE_{sd}, the 6-hour, KE_{6h}, nor the 3-hour KE_{3h} signals.

4.2.2. Power Spectra

The APE and KE power spectra were calculated by Fourier-transforming the time series at each depth, and averaging over all depths. The biggest peak in both the APE and KE power spectra occurs at the semidiurnal frequency, revealing the presence of near-inertial waves and/or a semidiurnal internal tide. Both the APE and KE power spectra reveal similar results. To save space, just the KE power spectra have been plotted, as can be seen in Figure 10.

The power spectra have been compared to the Garrett-Munk (GM) spectra (Garrett & Munk, 1972, 1975), which, as can be seen in Figure 10, are more energetic than the observed spectra. The total variance for the GM potential energy spectrum, which according to Parseval's Theorem is equivalent to the area under the power spectral curve, is on the order of 10^{-5} m^2/s^2, compared to the total variance in the observed potential energy spectra which are all on the order of 10^{-7} m^2/s^2. The total GM kinetic energy variance is on the order of 10^{-3} m^2/s^2, while the total variance in the observed kinetic energy spectra are all on the order of 10^{-5} m^2/s^2, which indicates a reduction in energy by a factor of about .01. These results are consistent with those of other Arctic experiments, which exhibit lower internal wave energy when compared with that of lower latitudes (i.e. Levine et al., 1985; Levine, 1990; Jardon et al., 2011; Fer et al., 2003, 2004, 2010). Levine et al. (1985) and Levine (1990), who find the Arctic wave field less energetic by an order of .02, attribute this reduced internal wave energy in the Arctic to the ice cover which reduces the wind forcing, increases momentum loss due to internal ice stress, and dampens the internal wave field due to the turbulent boundary layer beneath the ice. Along with the ice cover, Levine et al. (1985) and Levine (1990) also cite the weak circulation of the Arctic Ocean, as well as the fact that at higher latitudes, the internal tide is evanescent and not able to propagate as free waves, as possible explanations for this reduced internal wave energy.

While the observed power spectra are not as energetic as the GM spectra, by a factor of about .01, the shape and slope of the power spectra are similar to those of Garrett and Munk. To find the slope of the observed spectra, we fit the spectra to a simple power law fit plus constant noise, $A * f^{exp} + noise$, and found the slopes to range from -2.05 for April 2006, to -2.09 for April 2005, to -2.37 for April 2007, and -2.41 for May 2006, which are all comparable to the -2 slope of the GM spectrum.

4.3. Vertical Modes

To determine the vertical structure of the internal wave field, we project the measured velocity on the vertical modes. The modal components of the velocity were then used to calculate the KE for each mode. In Figure 11, we compare the percentage of KE per mode for the first ten modes for the total baroclinic kinetic energy (KE_{bc}), the semidiurnal kinetic energy (KE_{sd}), and the baroclinic perturbation kinetic energy (KE'_{bc}) for each time series.

As can be seen in Figure 11, mode 1 is the dominant mode of the total baroclinic kinetic energy (KE_{bc}) for all four time series. During April 2005 and April 2007, however, approximately 90% of the KE_{bc} is in mode 1, which is similar to the response we would expect in a two-layer fluid, where all the energy is in mode 1. This mode-1 response can be attributed to the very strong pycnoclines evident in the April 2005 and April 2007 N^2 profiles (Figure 3a and b), and their associated high γ values of 0.62 and 0.65 respectively, which indicate a stratification profile similar to that of a two-layer fluid (see Section 3.2). While mode 1 is also the dominant mode for KE_{bc} during April 2006 and May 2006, it accounts for only 50% of KE_{bc} for May 2006 and only 30% for April 2006, which corresponds to their low γ values of 0.32 and 0.16 respectively.

If, however, we break $\mathbf{U}_{bc}$ down, and look at the modal decomposition of the KE of the time-mean currents and that of the baroclinic perturbation velocities (KE'_{bc}) separately, we find that the mode-1 dominance seen in $\mathbf{U}_{bc}$ is due mostly to its time-mean current. The mode-1 dominance of the time-mean KE is particularly strong for April 2005, for which 99% of the time-mean KE is in mode 1, whereas only 88% of the time-mean KE for April 2007 is in mode 1, and less than 70% for May 2006 and April 2006. The KE of just the semidiurnal component of the internal waves, KE_{sd}, shows a similar distribution of energy by mode. For April 2005, while most of KE'_{bc} and KE_{sd} energy is still in mode 1, the energy is spread out over several modes, demonstrating that the energy is not purely mode 1 as it would be in a two-layer fluid, but rather lies on the spectrum between a pure two-layer fluid and a fluid of constant stratification, falling very close to the side of the two-layer fluid, which is consistent with its high γ value of 0.62.

If we look at KE'_{bc} and KE_{sd} for April 2006, we see that the energy is almost evenly distributed among the first five modes. So, on the spectrum between a fluid of constant stratification and that of a two-layer fluid, the stratification profile in April 2006 falls closer to a fluid of constant stratification, which favors an even distribution of energy over all modes. This is consistent with April 2006's low γ value of 0.16. KE'_{bc} and KE_{sd} for May 2006 similarly show peaks in other modes, but in this case, there is strong dominance in three particular modes, modes 1, 3, and 5, indicating that, while the modal response in May 2006 is far from purely mode-1, it is closer than that of April 2006, and thus lies more in the center of the spectrum between a fluid of constant stratification and that of a two-layer fluid, as predicted by its moderate γ value of 0.32.

5. Mixing

Turbulent mixing of the water column changes the distribution of physical water properties such as heat and salt. To get an insight into how much turbulent mixing we expect during each of our time series, we calculate the Richardson number, $Ri = N^2/S^2$, where S^2 is the shear squared ($S^2 = [(du/dz)^2 + (dv/dz)^2]$). Ri gives a measure of the likelihood that a stratified water column will undergo shear instability by balancing the stabilizing effects of the stratification, N^2, against the destabilizing effects of the shear, S^2. Smaller Ri reflects, therefore, a less stable water column, with typical critical values for expected shear instability ranging from 0.2 to 1 (Galperin et al., 2007).

The Ri values for our time series, as can be seen in Figure 12, reveal areas of anticipated instabilities at different points in the water column for each time series. Low Ri values in May 2006 and April 2007 occur at specific depths, concentrated on or just above the pycnoclines during these time series (see also Figure 3). During both April 2005 and April 2006, the two periods with a surface mixed layer, low Ri values are concentrated in the mixed layer, as expected. Below the mixed layer during these two time periods, low Ri values occur throughout the water column with no specific depth-dependence. The incidence of low Ri values is substantially greater in April 2006 than in April 2005. The greater occurrence of low Ri values in April 2006 is consistent with its low γ value, which indicates more energy in higher modes and thus a greater tendency for shear instabilities.

Once we have an idea of where we expect the water column to undergo shear instabilities, we determine how much turbulent kinetic energy is dissipating locally at each station. Since we do not have any simultaneous microstructure measurements, we cannot directly quantify the turbulent dissipation rate during the time series. We can, however, look at some larger-scale parameters, including stratification and shear, to get an approximation of the magnitude of the mixing generated by the internal wave field, based on dimensional scaling and fine-scale parameterizations.

5.1. Dimensional Scaling and Fine-Scale Parameterizations

Dimensional Scaling

Thorpe scale dimensional analysis (Thorpe, 2005) approximates the overall turbulent mixing based on the RMS length of observed density overturns, the Thorpe length, L_{Th}, and a linear relationship between L_{Th} and the outer scale of the turbulence, the Ozmidov length, L_O:

$$L_{Th} = c_1 L_O,$$

where c_1 is a constant that ranges from $.63 - .91$ (Thorpe, 2005). L_O is the length scale of vertical displacements that occur as turbulent kinetic energy is converted into potential energy, which scales like $L_O = (\epsilon N^{-3})^{\frac{1}{2}}$. L_{Th} is determined by comparing the actual density profiles with profiles sorted so the density is ascending with depth. Based on Thorpe-scale analysis, the rate of turbulent dissipation, hereinafter ϵ_{Th}, can be determined by:

$$\epsilon_{Th} = c_1 L_{Th}^2 (N_{ot}^3) [W kg^{-1}]$$

where N_{ot} is the average sorted stratification within the overturn. To keep our estimate of turbulent dissipation consistent with other estimates in Storfjorden, we have used $c_1 = 0.64$, following Jardon et al. (2011). To isolate overturns due to turbulence from those due to noise in the signal, we determined the noise level by comparing our spectra to an idealized spectrum composed of the GM spectrum plus a noise spectrum, which yields a density noise level on the order of $10^{-4}\ kg/m^3$, and followed the method laid out in Ferron et al. (1998) to eliminate any spurious overturns due to noise.

Fine-Scale Parameterizations

While Thorpe-scale analysis determines the rate of turbulent dissipation by dimensional scaling of larger-scale turbulent overturns, fine-scale parameterizations, such as the Gregg-Henyey (GH) parameterization (Gregg, 1989) and the MacKinnon-Gregg (MG) parameterization (MacKinnon & Gregg, 2003, 2005), determine the rate of turbulent dissipation based on the eikonal wave-wave interaction model and the assumption that the spectral shape of the internal wave field is in a steady state. GH, the most germaine of these fine-scale parameterizations, is based on comparison between empirical open-ocean data, and the Garrett-Munk (GM) model. The rate of turbulent dissipation determined by GH, hereinafter ϵ_{GH}, scales the fourth power of the observed 10-m shear with that of GM. Since our internal wave power spectra have similar shape and slope to the GM power spectrum, we have used this parameterization to estimate the rate of turbulent dissipation, ϵ_{GH}:

$$\epsilon_{GH} = 1.8 \times 10^{-6}[f cosh^{-1}(N_0/f)](S_{10}^4/S_{GM}^4)(N^2/N_0^2)[Wkg^{-1}],$$

where S_{GM} is the modeled 10-m Garrett-Munk shear, and $S_{GM}^4 = 1.66 \times 10^{-10}(N^2/N_0^2)^2[s^{-2}]$, S_{10} is the shear at 10-m resolution, f is the Coriolis frequency, which at our latitude is approximately $1.426 \times 10^{-4}[s^{-1}]$, and $N_0 = 3$ [cph].

While GH was intended to parameterize waves in the open ocean, MG modifies GH for low-mode dominated coastal regions, as is the case with our Storfjorden stations. As opposed to the GH scaling, which relies on 10-m resolution shear scaled by the GM shear variance, the turbulent rate of dissipation determined by MG, hereinafter ϵ_{MG}, relies on 1-m resolution low-frequency mode-1 shear. For consistency, we have used the same 4-m shear to calculate both ϵ_{MG} and ϵ_{GH}, as opposed to (S_{10}), following MacKinnon & Gregg (2003). To quantify the shear in the most precise manner possible, we have computed the vertical derivative in spectral space by periodizing the 4-m resolution ADCP velocity and taking the inverse Fourier transform. For consistency, the 4-m observed shear, S_4, is scaled by the 4-m GM shear S_{4GM} (Klymak, 2012). Using the 4-m shear of the entire velocity field, we have employed a modified version of MG:

$$\epsilon_{MG} = \epsilon_0(N/N_0)(S_4/S_0)[Wkg^{-1}],$$

where $S_0 = N_0 = 3$ [cph], and ϵ_0 is an adjustable parameter found by fitting ϵ_{MG} to simultaneous microstructure measurements. Since we do not have simultaneous microstructure measurements, however, we cannot use them to adjust our ϵ_0. Working under the assumption that "when overturns are observed, the dissipation rates calculated from ϵ_{Th} are roughly the same magnitude as the rates calculated from microstructure," (MacKinnon & Gregg, 2005), we take the time series that has overturns consistently throughout the water column, April 2007, and fit our ϵ_{MG} to our ϵ_{Th} using a least squares fit to find the value of ϵ_0. While there is no defined mixed layer in April 2007, if we fit only the ϵ_{Th} values below the pycnocline depth (defined in Section 3.2), we can limit the overturns due to surface processes. We find $\epsilon_0 = 4.6 \times 10^{-9} W kg^{-1}$, which is the same order of magnitude as MacKinnon & Gregg (2005), whose $\epsilon_0 = 1.1 \times 10^{-9} W kg^{-1}$.

To compare the contributions to mixing due to the baroclinic field perturbations, and those due to the total baroclinic field, we have calculated ϵ_{MG} and ϵ_{GH} using both the $\mathbf{U}'_{bc}$ shear, and the $\mathbf{U}_{bc}$ shear. Since these parameterizations are based on wave-wave interactions in the stratified water column, they have only been applied below the mixed layer for the two time series with mixed layers (April 2005 and April 2006).

Once we have found the rate of turbulent dissipation, ϵ, we use that to find the rate of diapycnal diffusivity, κ_z. Assuming that turbulence is stationary, we can define the relationship between ϵ and κ_z as

$$\kappa_z = \Gamma \epsilon / N^2, \tag{1}$$

where Γ is known as the mixing efficiency. Osborn (1980) found that the upper bound for Γ is 0.2 and this value is commonly used to determine κ_z from ϵ. Several recent studies, however, have also shown that the mixing efficiency is not a constant, but rather decreases with the turbulence intensity, I, which is defined as:

$$I = \frac{\epsilon}{\nu N^2},$$

where ν is the kinematic viscosity of water. I can be seen as the ratio of the stabilizing effects of viscosity and stratification against the destabilizing effects of turbulence. Using high-resolution numerical simulations of stratified turbulence, Shih et al. (2005) have proposed empirical laws to parameterize κ_z as a function of I. They define three regimes: In the diffusive range where the turbulent intensity is low, the total diffusivity reverts to the molecular value, $\kappa_T = 1 \times 10^{-7} m^2/s$. If the turbulent intensity is in an intermediate range between 7 and 100, κ_{turb} is defined by the Osborn (1980) relation,

$\kappa_{turb} = \frac{\Gamma\epsilon}{N^2}$, with $\Gamma = 0.2$. If, however, the turbulent intensity is elevated above 100, $\kappa_{turb} = 2\nu I^{\frac{1}{2}}$. The turbulent intensities in our data range from $I \approx 1$ to $I \approx 600$, with the majority lying in the intermediate range. The total κ_z is then found by adding $\kappa_{turb} + \kappa_T$.

5.2. Mixing Estimates

In order to compare the relative mixing between our four stations with their four distinct stratification profiles, we have calculated both the MG and GH fine-scale parameterizations, and indicated the average values, along with the 95% confidence intervals, in Table 1.

MG yields an overall average ϵ estimate for the $\mathbf{U}_{bc}$ field (ϵ_{MG}) of $5 \times 10^{-9} Wkg^{-1}$. The average ϵ_{MG} for each time series varies slightly, ranging from 3 to $7 \times 10^{-9} Wkg^{-1}$ for the $\mathbf{U}_{bc}$ field, with the average values dropping slightly to 2 to $5 \times 10^{-9} Wkg^{-1}$ for the $\mathbf{U}'_{bc}$ field (Table 1). ϵ_{GH} estimates are of the same order as ϵ_{MG}, with an overall average value of $6 \times 10^{-9} Wkg^{-1}$. The average ϵ_{GH} for each time series, however, reveal greater differences between the time series, with values ranging from $1.2 \times 10^{-9} Wkg^{-1}$ in April 2005 to $1.1 \times 10^{-8} Wkg^{-1}$, an order of magnitude greater, in May 2006. If we look at the average ϵ_{GH} values based on just the $\mathbf{U}'_{bc}$ field (ϵ'_{GH}), the ranking is consistent with the γ value for each time series (see Section 3.2), with the two time series with the greatest γ values, April 2005 and April 2007, having the lowest ϵ'_{GH} values of $1.0 \times 10^{-9} Wkg^{-1}$. The two other time series with lower γ values, May 2006 and April 2006, have higher ϵ'_{GH} values, on the order of $6 \times 10^{-9} Wkg^{-1}$, as can be seen in Table 1.

Figure 13 compares the time-mean ϵ_{MG} and ϵ_{GH} calculated from $\mathbf{U}_{bc}$, hereinafter ϵ_{bc}, and $\mathbf{U}'_{bc}$, hereinafter ϵ'_{bc}. The two time series with the biggest drop between ϵ_{bc} and ϵ'_{bc} are April 2007, whose mean ϵ_{GH} drops from $6.1 \times 10^{-9} Wkg^{-1}$ to $1.0 \times 10^{-9} Wkg^{-1}$ for ϵ'_{GH}, and whose mean ϵ_{MG} drops from $7.0 \times 10^{-9} Wkg^{-1}$ to $2.3 \times 10^{-9} Wkg^{-1}$ for ϵ'_{MG}. May 2006 shows a similar drop between ϵ_{bc} and ϵ'_{bc}, with a drop in ϵ_{GH} from $1.1 \times 10^{-8} Wkg^{-1}$ to $5.6 \times 10^{-9} Wkg^{-1}$, and a drop in ϵ_{MG} from $4.8 \times 10^{-9} Wkg^{-1}$ to $2.2 \times 10^{-9} Wkg^{-1}$ (Table 1). In contrast, April 2005 shows a much smaller drop between ϵ_{bc} and ϵ'_{bc}, with its mean ϵ_{GH} dropping slightly from 1.2 to $1.0 \times 10^{-9} Wkg^{-1}$, and mean ϵ_{MG} from 5.7 to $5.0 \times 10^{-9} Wkg^{-1}$. This small difference corresponds to the fact that while there is a marked drop in energy from the total KE_{bc} to the total KE'_{bc} for April 2005 (see Section 4.3), nearly all of the time-mean KE is in mode 1, so there is little loss of shear between $\mathbf{U}_{bc}$ and $\mathbf{U}'_{bc}$. Similarly, the mean ϵ_{GH} for April 2006 drops only slightly from 6.9 to 6.3

$\times\ 10^{-9} W kg^{-1}$, and the mean ϵ_{MG} of $3.4 \times 10^{-9} W kg^{-1}$ remains practically unchanged, as can be seen in Figure 13. The fact that these two time series show little to no change between ϵ_{bc} and ϵ'_{bc}, indicates that the shear during these two periods is due almost entirely to internal waves. Note that we have displayed the Thorpe scale estimates in Figure 13 as well, but the reader must not look for point-to-point comparison. We expect the Thorpe scale and the finescale parameterizations to have the same range of variation, and that the overall average values are of the same order, as they are, but we do not expect the values to be equivalent, since Thorpe scale estimates are instantaneous values, while the fine-scale parameterized values are averaged over at least twelve hours.

While the average ϵ values in Figure 13 allow us to compare the relative strength of the average ϵ in each time series, the probability distribution functions, as represented in Figure 14, allow us to compare all the data. The time series with the highest ϵ_{bc} values in Figure 14 is April 2007, with mode values an order of magnitude greater than the other time series. When the parameterizations are calculated solely on $\mathbf{U}'_{bc}$, however, April 2007 has the greatest shift in ϵ, indicating that most of the turbulent dissipation in this time series is due to contributions from low-frequency signals, with a period greater than 6 hours. The time series with the smallest difference between ϵ_{bc} and ϵ'_{bc} is April 2006, and in fact the mode values for both ϵ'_{MG} and ϵ'_{GH} are greater than or equal to all the other time series, indicating that while there is much less turbulent dissipation due to low-frequency signals in this time series, there is much greater dissipation due to internal waves.

To understand how these different turbulent rates of dissipation, ϵ, affect the mixing during each time series, we compare the diapycnal diffusivities, κ_z, both those due to $\mathbf{U}_{bc}$, hereinafter κ_z, and those due to $\mathbf{U}'_{bc}$, hereinafter κ'_z, as seen in Figure 15. The overall average κ_z for both GH and MG are 5.7×10^{-4} and $1.3 \times 10^{-4}\ m^2 s^{-1}$, respectively, dropping to 4.1×10^{-4} and $5.2 \times 10^{-5}\ m^2 s^{-1}$ for κ'_z. The relative strength of κ_{zGH} and $\kappa_z{}'_{GH}$ for each time series is consistent with their different γ values, with the greatest values occurring in April 2006 and May 2006, and the lowest values occurring in April 2007 and April 2005. The high γ values in April 2005 and April 2007 correspond to lower diapycnal diffusivities, associated with lower rates of turbulent dissipation. In contrast, the higher diapycnal diffusivities in April 2006 are most likely due to its low γ value, and corresponding higher rates of turbulent dissipation.

Heat Flux

To get a better idea of the impact of turbulent mixing on the local ocean-ice heat budget, we use the diapycnal diffusivities to calculate the vertical heat flux, $Q = -\rho c_p \kappa_z \delta_z T$. The resultant local change in temperature due to this heat flux, $\delta_t T = -\frac{1}{\rho c_p} \delta_z Q$, is then evaluated. The vertical heat flux, Q, both due to κ_z, and κ'_z, for the three time series with concurrent CTD and ADCP measurements, can be seen in the top three plots of Figure 16. During both April 2005 and April 2006, Figure 16a and b, there is a net downward heat flux below the mixed layer for both $\mathbf{U}_{bc}$ and $\mathbf{U}'_{bc}$, whereas May 2006, Figure 16c, reveals a net upward heat flux.

The three lower plots in Figure 16 depict the local heating and cooling associated with these vertical heat fluxes. There is a complex pattern of both heating and cooling occurring throughout the water column for all time series, on the order of 10^{-2} $^{o}K/month$. The spatial pattern is similar to that of the heat flux with most of the activity occurring near the top the pycnocline for each time series. In April 2006 there is a net cooling in the first half of the time series, followed by a net heating in the second half of the time series. May 2006 reveals the opposite pattern with a net heating followed by a net cooling in the top of the water column and an associated heating in the bottom of the water column. Since our time series are too short to notice any long-term trends, however, further investigation is necessary to explore the possible effects of different stratification profiles on long-term heating or cooling in Storfjorden.

6. Discussion

In this isolated Arctic fjord, these four time periods in three subsequent springs exhibit notably different stratification (N^2) profiles. Two of the time series have sharp pycnoclines and associated high Gerkema (2001) γ values, while one time series has a nearly constant stratification profile, and a very low γ value, and one lies between these two extremes, with an intermediate γ value.

These different stratification regimes impact the dynamics and energetics of the internal waves during each time series. While mode 1 is the dominant mode of the baroclinic kinetic energy (KE_{bc}) for all the time series, for the two high γ-value time series, approximately 90% of KE_{bc} is in mode 1, similar to that of a two-layer fluid, where all the energy is in mode 1. For the time series with the smallest γ value, just 30% of KE_{bc} is in mode 1, similar to that of a fluid of constant stratification, where none of the energy is in mode 1, and for the intermediate γ-value time series, 50% of KE_{bc} is in mode 1, indicating that it lies on the spectrum between a two-layer fluid, and one of constant stratification.

The differences in stratification profiles impact not only the dynamics, but also the dissipation of the internal waves at each station. Both the Gregg-Henyey (GH) and MacKinnon-Gregg (MG) fine-scale parameterizations yield similar estimates for the turbulent rate of dissipation (ϵ), with an overall average ϵ of $5-6 \times 10^{-9} W kg^{-1}$. These values, obtained during ice-covered conditions, are an order of magnitude below microstructure and fine-scale approximations obtained during a period of open water in Storfjorden (Fer, 2006). The relative rate of turbulent dissipation predicted by GH, ϵ_{GH}, varies considerably among the time series, with lower turbulent dissipation predicted for the high-γ value time series (Table 1). When we look at just the ϵ'_{bc} predicted by GH, the estimates for ϵ are consistent with the γ values for the various time series. Lower estimated ϵ'_{GH} occurs during the two high γ-value time series, and higher estimated ϵ'_{GH} occurrs during the low and intermediate γ-value time series (Table 1).

The most direct association with the stratification profiles is with the diapycnal diffusivities (κ_z), or mixing, of the different time series. The two high γ-value time series have the lowest diapycnal diffusivities predicted by GH (κ_{zGH}, and κ'_{zGH}), and the highest diapycnal diffusivities are seen during the period with the low γ-value time series. The intermediate γ-value time series has intermediate mixing values (Table 1). Note that, since the internal wave signal is the dominant signal in our data, we have focused on mixing due to internal waves. There is, however, also a strong subinertial signal, particularly during the higher-γ value time series (see Figure 7). While our data set does not allow us to determine the source of this energy, possible sources include surface water run-off induced estuarine circulation, wind forcing, and convection due to brine rejection.

Differences in the estimated heat flux and the associated local heating and cooling do not, however, correspond to differences in stratification profiles. While the heat flux is calculated from the diapycnal diffusivities, it is strongly dependent on the temperature gradient. Since the stratification in Storfjorden is mostly controlled by the salinity, and not the temperature, there is no direct relation between the stratification profiles and the temperature gradients, and thus no direct relation between the turbulent dissipation rate and the turbulent heat flux. In fact, the greatest heat flux occurs during one of the high γ-value time series, and the lowest heat flux occurs during the low γ-value time series, the inverse of what we would expect were the turbulent dissipation rate and the turbulent heat flux directly related.

When averaged over a whole number of inertial periods, the maximum net heat flux intensities resulting from internal wave-induced mixing were found at the tops of the pycnoclines and typically reached $1Wm^{-2}$ in the intermediate γ-value time series, and $-1Wm^{-2}$ in the high γ-value time series, which is about two orders of magnitude smaller than typical heat flux at the air-sea interface of open polynyas, but still comparable to typical heat flux during ice-covered conditions (McPhee et al., 2013). Note that these weak heat fluxes could help explain the persistence of supercooled water several days after its formation in strongly mixed conditions, as observed by Jardon et al. (2014) and McPhee et al. (2013).

7. Conclusion

Based on our results, we can infer that the shape of the stratification profile is a controlling factor on the dynamics and dissipation of internal waves. While the magnitude of the average stratification may remain relatively unchanged, the shape and characteristics of the stratification profile can vary rapidly in the Arctic. The more closely an N^2 profile resembles that of a two-layer fluid, as defined by its γ value, the more it is dominated by a mode-1 response. High γ-value time series have more energy in mode 1 of the baroclinic time mean currents, and thus less energy in the higher modes of $\mathbf{U}'_{bc}$. With less energy in the higher modes, these high γ-value time series have lower rates of turbulent dissipation, and lower diapycnal diffusivities. The more closely an N^2 profile resembles that of a fluid of constant stratification, however, the more it is dominated by higher modes and vertical propagation. These low γ-value time series have less energy in the baroclinic time-mean current, and more energy in the higher modes of $\mathbf{U}'_{bc}$. Since more of the energy is found in the higher modes, low γ-value regimes have higher rates of turbulent dissipation, and higher diapycnal diffusivities.

This effect could play an important role in how circulation models parameterize mixing. Since models do not resolve the higher modes, they rely on the assumption that more energy leads to proportionately higher diapycnal diffusivities. This is in fact the opposite of what we have found in Storfjorden. During periods with high γ-value stratification profiles, more of the energy goes into mode 1, than goes into the higher modes, which are responsible for most of the turbulent diffusivity. There will therefore be less mixing than expected based on the energy level. During periods with low γ-value stratification profiles, the energy is more evenly distributed over the different vertical modes, including in the higher modes, resulting in greater mixing than expected based on the energy level. A parameterization that only considers the magnitude of the stratification, will thus tend to overestimate mixing in periods of high γ values, and underestimate it in periods of low γ values. When considering the impact of stratification on high latitude mixing, the magnitude should not be used alone, but rather should be considered in conjunction with the structure of the stratification profile.

Acknowledgments

We would like to thank Jean-Claude Gascard and his team for collecting the data for the three time series in 2005 and 2006 as part of the BRINES campaign, an IPEV-sponsored experiment (prog 417). Data from 2007 were collected during the ICE-DYN campaign funded by IPEV (prog 1058) and analyses were carried out as part of the OPTIMISM project (ANR-09-BLAN-0227-01; IPEV 1015). We would like to thank Eric Brossier and France Pinczon du Sel and the rest of the crew of the polar yacht Vagabond, supported by the DAMOCLES and BRINES programs, for their help during field work. The authors also acknowledge the NOAA/OAR/ESRL PSD, Boulder, Colorado, USA, for providing free and open access to NCEP Reanalysis Derived on their website at http://www.esrl.noaa.gov/psd/. Tamara Beitzel Barriquand was supported by a National Science Foundation Graduate Research Fellowship.

References

Baines, P. (1982). On internal tide generation models. *Deep-Sea Res.*, *29*, 307–338.

ECMWF (2014). European centre for medium-range weather forecasts ecmwf era-40 re-analysis data.

Fer, I. (2006). Scaling turbulent dissipation in an arctic fjord. *Deep-Sea Res II*, *53*, 77–95.

Fer, I., & Drinkwater, K. (2014). Mixing in the Barents Sea Polar Front near Hopen in spring. *Journal of Marine Systems*, *130*, 206–218.

Fer, I., Skogseth, R., & Geyer, F. (2010). Internal waves and mixing in the marginal ice zone near the yermak plateau. *J. Phys. Oceanogr.*, *40*, 1613–1630.

Fer, I., Skogseth, R., & Haugan, P. M. (2004). Mixing of the storfjorden overflow (svalbard archipelago) inferred from density overturns. *J. Geophys. Res.*, *109*.

Fer, I., Skogseth, R., Haugan, P. M., & Jaccard, P. (2003). Observations of the storfjorden overflow. *Deep-Sea Res. I*, *50*, 1283–1303, doi: 10.1016/S0967–0637(03)00124–9.

Ferron, B., Mercier, H., Speer, K., Gargett, A., & Polzin, K. (1998). Mixing in the Romanche Fracture Zone. *J. Phys. Oceanogr.*, *28*, 1929–1945.

Galperin, B., Sukoriansky, S., & Anderson, P. A. (2007). On the critical Richardson number in stably stratified turbulence. *Atmospheric Science Letters*, *8*, 65–69.

Garrett, C., & Munk, W. (1972). Space-time scales of internal waves. *Geophys. Fluid Dyn.*, *2*, 225–264.

Garrett, C. J. R., & Munk, W. H. (1975). Space-time scales of internal waves: A progress report. *J. Geophys. Res.*, *80*, 291–297.

Gerkema, T. (2001). Internal and interfacial tides: Beam scattering and local generation of solitary waves. *J. Mar. Res.*, *59*, 227–255.

Gerkema, T., & van Haren, H. (2007). Internal tides and energy fluxes over great meteor seamount. *Ocean Sci.*, *3*, 441–449.

Gerkema, T., & Shrira, V. I. (2005a). Near-inertial waves in the ocean: beyong the 'traditional approximation'. *J. Fluid Mech.*, *529*, 195–219, doi:10.1017/S0022112005003411.

Gerkema, T., & Shrira, V. I. (2005b). Near-inertial waves on the "nontraditional" β plane. *J. Geophys. Res.*, *110*, doi:10.1029/2004JC002519.

Gregg, M. (1989). Scaling turbulent dissipation in the thermocline. *J. Geophys. Res.*, *94*, 9686–9698.

Guthrie, J. D., Morrison, J. H., & Fer, I. (2013). Revisiting internal waves and mixing in the arctic ocean. *J. Geophys. Res.*, *118*, 1–12.

Jardon, F., Bouruet-Aubertot, P., Cuypers, Y., Vivier, F., & Laurenço, A. (2011). Internal waves and vertical mixing in the storfjorden polynya, svalbard. *J. Geophys. Res.*, *116*, doi:10.1029/2010JC006918.

Jardon, F., Vivier, F., Bouruet-Aubertot, P., Laurenço, A., Cuypers, Y., & Willmes, S. (2014). Ice production in Storfjorden (Svalbard) estimated from a model based on AMSR-E observations: impact on water masses properties. *J. Geophys. Res.*, *119*, 377–393, doi:10.1002/2013JC009322.

Kalnay (1996). The NCEP/NCAR 40-year reanalysis project. *Bulletin of the American Meteorological Society*, *77*, 437–470.

Klymak, J. (2012). The garrett and munk internal wave spectra matlab toolbox.

Levine, M. D. (1990). Internal waves under the arctic pack ice during the arctic internal wave experiment: The coherence structure. *J. Geophys. Res.*, *95*, 7347–7357.

Levine, M. D., Paulson, C. A., & Morison, J. H. (1985). Internal waves in the arctic ocean: Comparison with lower-latitude observations. *J. Phys. Ocean.*, *15*, 800–809.

Loeng, H. (1991). Features of the physical oceanographic conditions of the barents sea. *Polar Research*, *10*, 5:18.

MacKinnon, J., & Gregg, M. (2003). Mixing on the late-summer New England shelf – solibores, shear and stratification. *J. Phys. Oceanogr.*, *33*, 1476–1492.

MacKinnon, J., & Gregg, M. (2005). Spring mixing: tubulence and internal waves during restratification on the New England shelf. *J. Phys. Oceanogr.*, *35*, 2425–2443.

McPhee, M. G., Skogseth, R., Nilsen, F., & Smedsrud, L. H. (2013). Creation and tidal advection of a cold salinity front in storfjorden: 2. supercooling induced by turbulent mixing of cold water. *J. Geophys. Res.*, *118*, 3737–3751, doi:10.1002/jgrc.20261.

Mercier, M. J., Mathur, M., Gostiaux, L., Gerkema, T., Magalhães, J. M., Silva, J. C. D., & Dauxois, T. (2012). Soliton generation by internal tidal beams impinging on a pycnocline: laboratory experiments. *J. Fluid Mech.*, *704*, 37–60.

Osborn, T. R. (1980). Estimates of the local rate of vertical diffusion from dissipation measurements. *J. Phys. Oceanogr.*, *10*, 83–89.

Padman, L., & Erofeeva, L. (2004). A barortropic inverse tidal model for the arctic ocean. *Geophys. Res. Lett.*, *31(2)*, doi:10.1029/2003GL019003.

PolarView (2012). Polar view – european arctic node.

Quadfasel, D., Rudels, B., & Kurz, K. (1988). Outflow of dense water from a svalbard fjord into the fram straight. *Deep-Sea Res.*, *35*, 1143–1150.

Schauer, U. (1995). The release of brine-enriched shelf water from storfjord into the norwegian sea. *J. Geophys. Res.*, *100*.

Shih, L., Koseff, J., Ivey, G. N., & Ferziger, J. H. (2005). Parameterization of turbulent fluxes and scales using homogeneous sheared stably stratified turbulence simulations. *J. Fluid Mech.*, *525*, 193–214.

Skogseth, R., Haugan, P., , & Jakobsson, M. (2005). Watermass transformations in Storfjorden. *Continental Shelf Research*, *25*, 667–695.

Skogseth, R., McPhee, M. G., Nilsen, F., & Smedsrud, L. H. (2013). Creation and tidal advection of a cold salinity front in Storfjorden: 1. Polynya dynamics. *J. Geophys. Res.*, *118*, 1–14, doi: 10.1002/jgrc.20231.

Sundfjord, A., Fer, I., Kasajima, Y., & Svendsen, H. (2007). Observations of turbulent mixing and hydrography in the marginal ice zone of the barents sea. *J. Geophys. Res.*, *112*.

Thorpe, S. A. (2005). *The Turbulent Ocean*. Cambridge Univ. Press.

Vlasenko, V., Stashchuk, N., Hutter, K., & Sabinin, K. (2003). Nonlinear internal waves forced by tides near the critical latitude. *Deep-Sea Res. I*, *50*, 317–338.

Winters, K. B., Bouruet-Aubertot, P., & Gerkema, T. (2011). Critical reflection and abyssal trapping of near-inertial waves on a β plane. *J. Fluid Mech.*, *684*, 111–136, doi: 10.1017/jfm.2011.280.

Table 1: Values of chosen parameters from each time series. Average wind speed and ice cover are shown in rows 2 and 3, respectively. The Gerkema (2001) γ parameter is shown in the fourth row, and the percentage of baroclinic KE in mode 1, in the fifth row. Rows 6-13 represent arithmetic mean values of ϵ and κ_z for both U_{bc} and U'_{bc} based on MG and GH parameterizations, with the 95% confidence intervals indicated in brackets.

time series	April 2005	April 2007	April 2006	May 2006
γ	.62	.65	.16	.32
winds $[m/s]$	.69	4.3	7.1	2.6
% ice cover	90-100%	100%	70-90%	100%
$\%KE_{bc}$ in Mode 1	91%	88%	31%	51%
ϵ_{GH} $[Wkg^{-1}]$	1.2e-9 [1.0 1.3]	6.1e-9 [5.3 6.8]	6.9e-9 [6.3 7.6]	1.1e-8 [.74 1.5]
ϵ'_{GH} $[Wkg^{-1}]$	1.0e-9 [.81 1.2]	1.0e-9[.84 1.2]	6.3e-9[5.7 7.0]	5.6e-9 [2.7 10]
ϵ_{MG} $[Wkg^{-1}]$	5.7e-9 [5.6 5.9]	7.0e-9 [6.6 7.2]	3.4e-9 [3.4 3.5]	4.8e-9 [4.6 5.0]
ϵ'_{MG} $[Wkg^{-1}]$	5.0e-9 [5.5 5.8]	2.3e-9 [2.3 2.4]	3.4e-9 [3.4 3.5]	2.2e-9 [2.1 2.2]
κ_{zGH} $[m^2s^{-1}]$	8.8e-5 [5.2 13]	2.6e-4 [2.1 3.3]	1.4e-3 [1.2 1.5]	6.2e-4 [3.8 9.2]
κ'_{zGH} $[m^2s^{-1}]$	8.4e-5 [5.2 12]	3.1e-5 [1.6 5.1]	1.2e-3 [1.1 1.4]	3.1e-4 [1.2 5.4]
κ_{zMG} $[m^2s^{-1}]$	5.0e-5 [4.7 5.5]	1.5e-4 [1.4 1.6]	1.6e-4 [1.5 1.6]	1.6e-4 [1.5 1.7]
κ'_{zMG} $[m^2s^{-1}]$	4.1e-5 [3.8 4.5]	6.5e-6 [5.5 8.3]	1.5e-4 [1.4 1.5]	1.5e-5 [1.3 1.8]

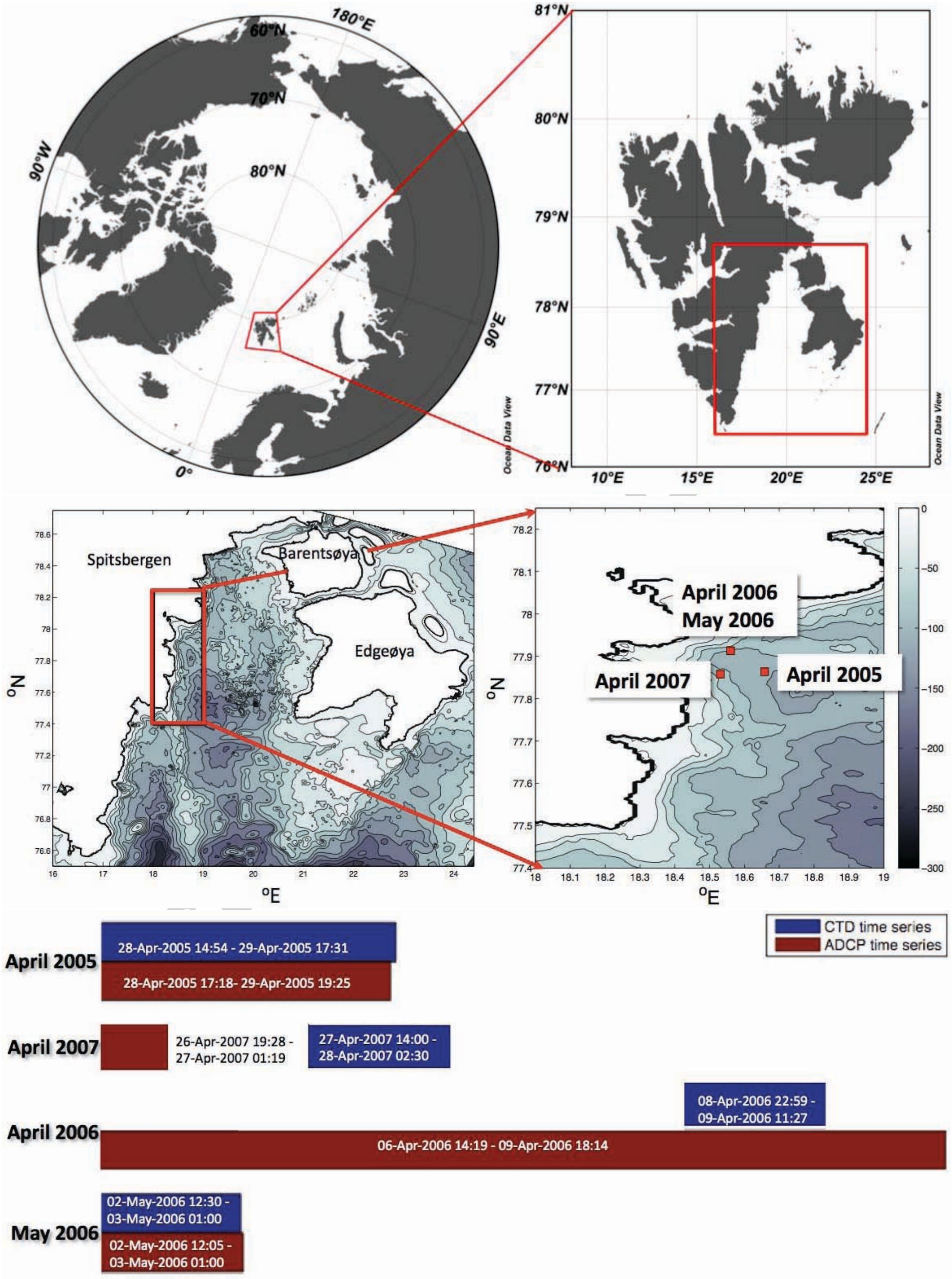

Figure 1: Global view of the Arctic Ocean and a blow-up of the Svalbard archipelago with a red box around Storfjorden (top) Overview of Storfjorden with a blow-up of the study area (middle). Red squares indicate locations of the three CTD/ADCP stations (April 2006 and May 2006 were co-located.) The relative length of the CTD (blue) and ADCP(red) time series are depicted (bottom).

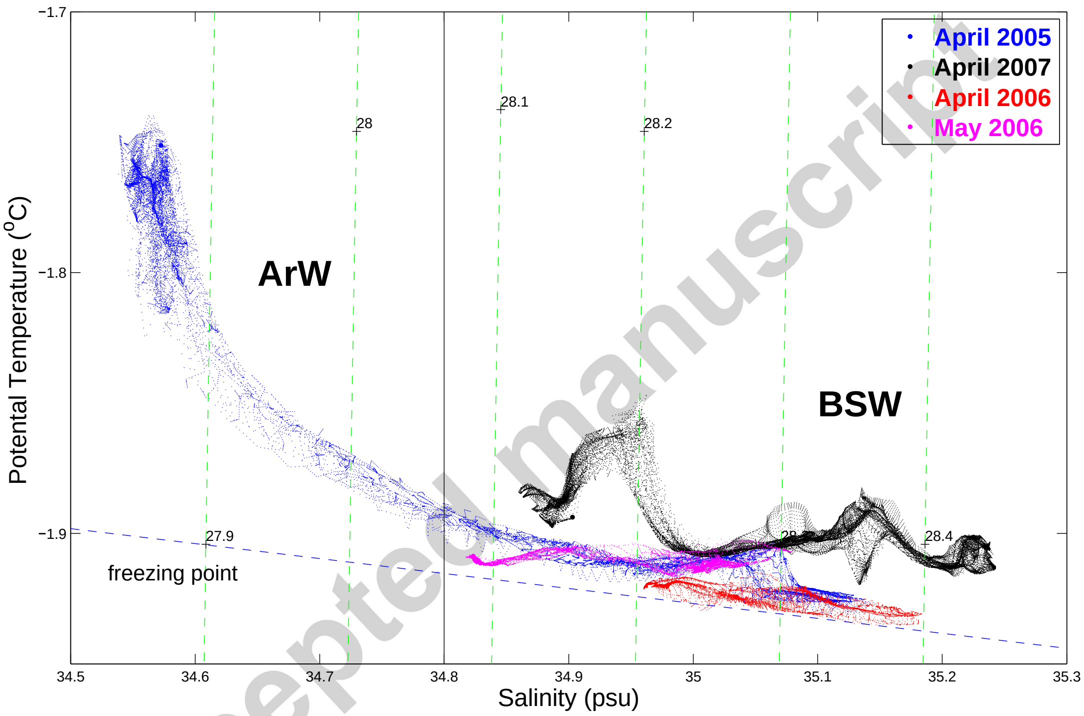

Figure 2: Potential Temperature-Salinity Diagrams from the four time series in Storfjorden. Different colors represent different time series. Dashed green lines trace surfaces of constant density, and the dashed blue line indicates the freezing point temperature. Water masses, based on the water mass classification by Loeng (1991) and Skogseth et al. (2005), are indicated.

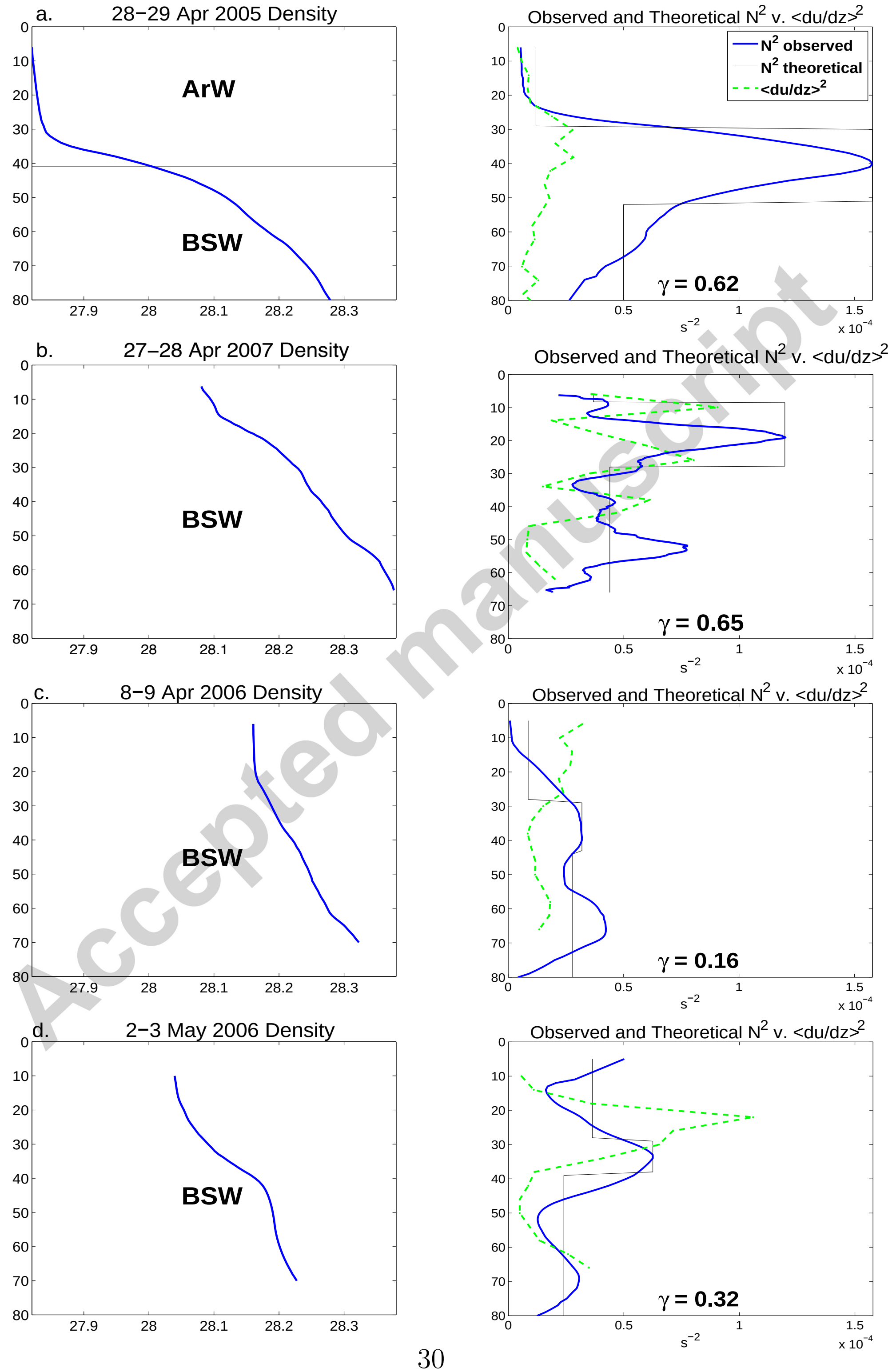

Figure 3: The time-mean density, as well as the sources of the water masses that make up the water columns (Loeng, 1991; Skogseth et al., 2005) are indicated for each profile (left). The time-mean squared shear, $\frac{d\mathbf{u}}{dz}^2$, (green) is compared to the time-mean squared Brunt-Vaisala frequency, N^2, (blue) for each profile (right). The fit to the theoretical Gerkema (2001) 2c-layer model (black), as well as the theoretical $\gamma = \frac{(g'd)^{1/2}}{N_c H}$ are also indicated for each profile (right).

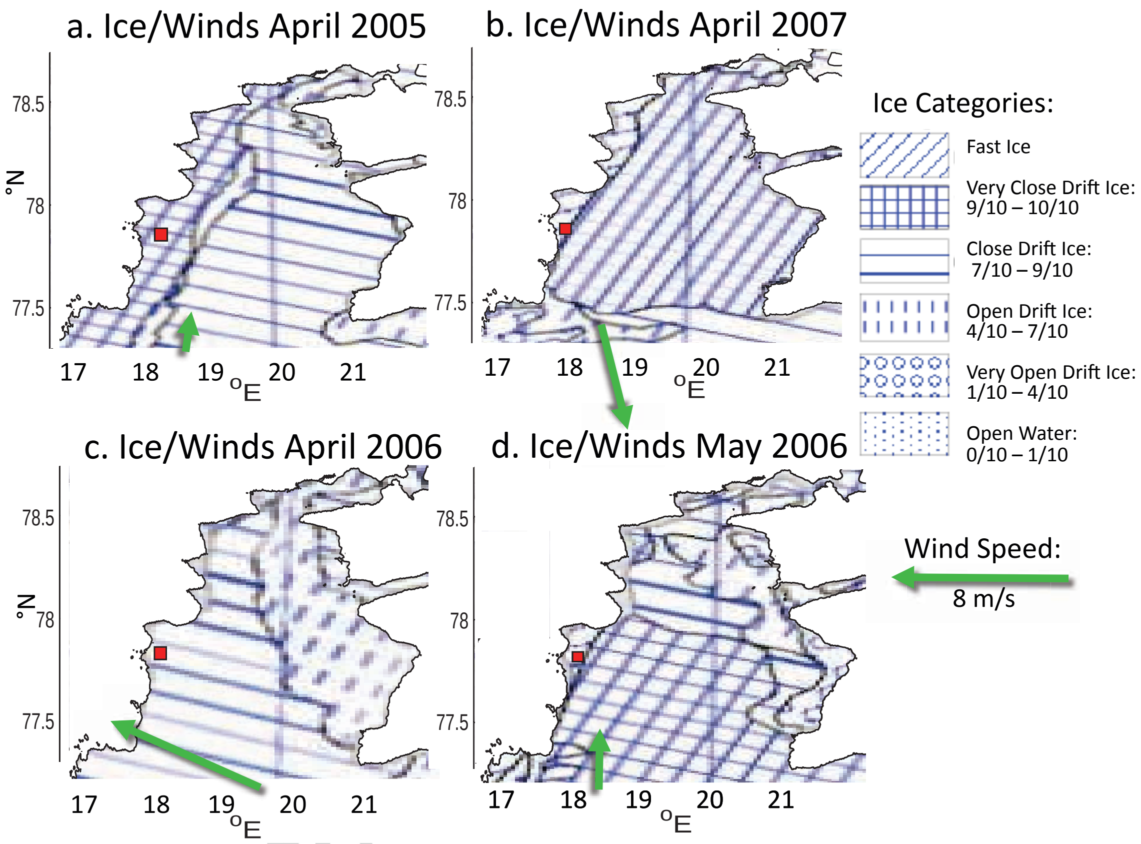

Figure 4: Ice charts in Storfjorden 28 April 2005 (a), 7 April 2006 (c), 2 May 2006 (d), and 27 April 2007 (b). These data come from the Meteorologisk institutt (PolarView, 2012). Both the April 2007 (b) and May 2006 (d) ice charts indicate "fast ice" or solid ice cover, along the western edge of Storfjorden near the CTD/ADCP stations, whereas both April 2005 (a) and April 2006 (c) icecharts indicate no "fast ice" along the western edge, but rather "very close drift ice" (90-100%) and "close drift ice" (70-90%), respectively. The green arrow represents the relative wind strength based on NCAR/NCEP Reanalysis data at 77.14° N, 18.75° E. The wind vectors represent the average wind values over each time series.

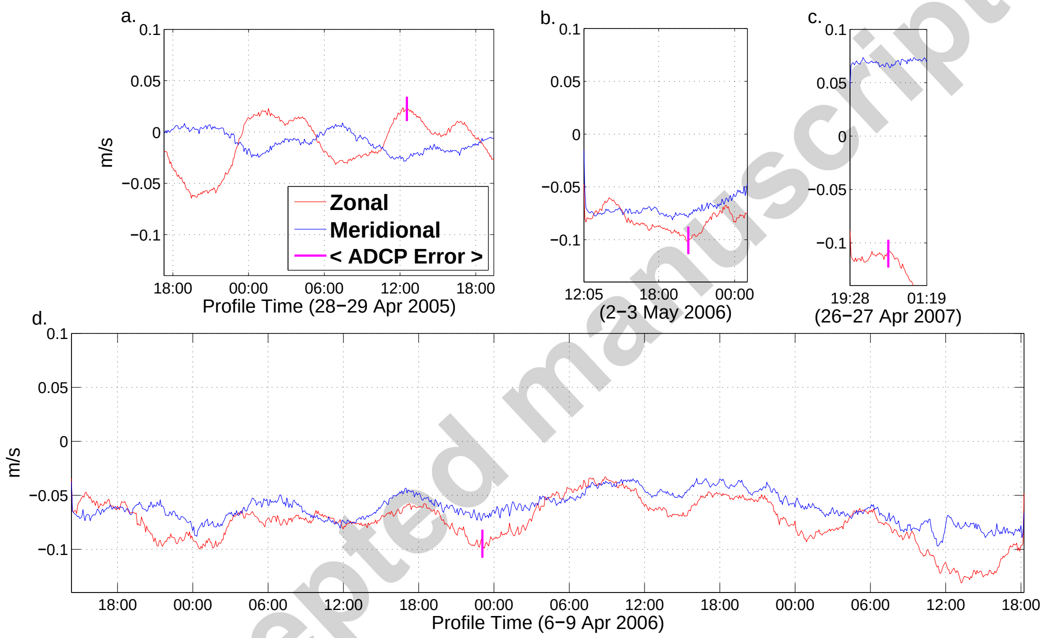

Figure 5: The barotropic (depth-mean) velocities (m/s) in both the zonal (blue) and meridional (red) directions for April 2005 (a), May 2006 (b), April 2007 (c), and April 2006 (d). The average barotropic ADCP error (magenta) is indicated for each time series.

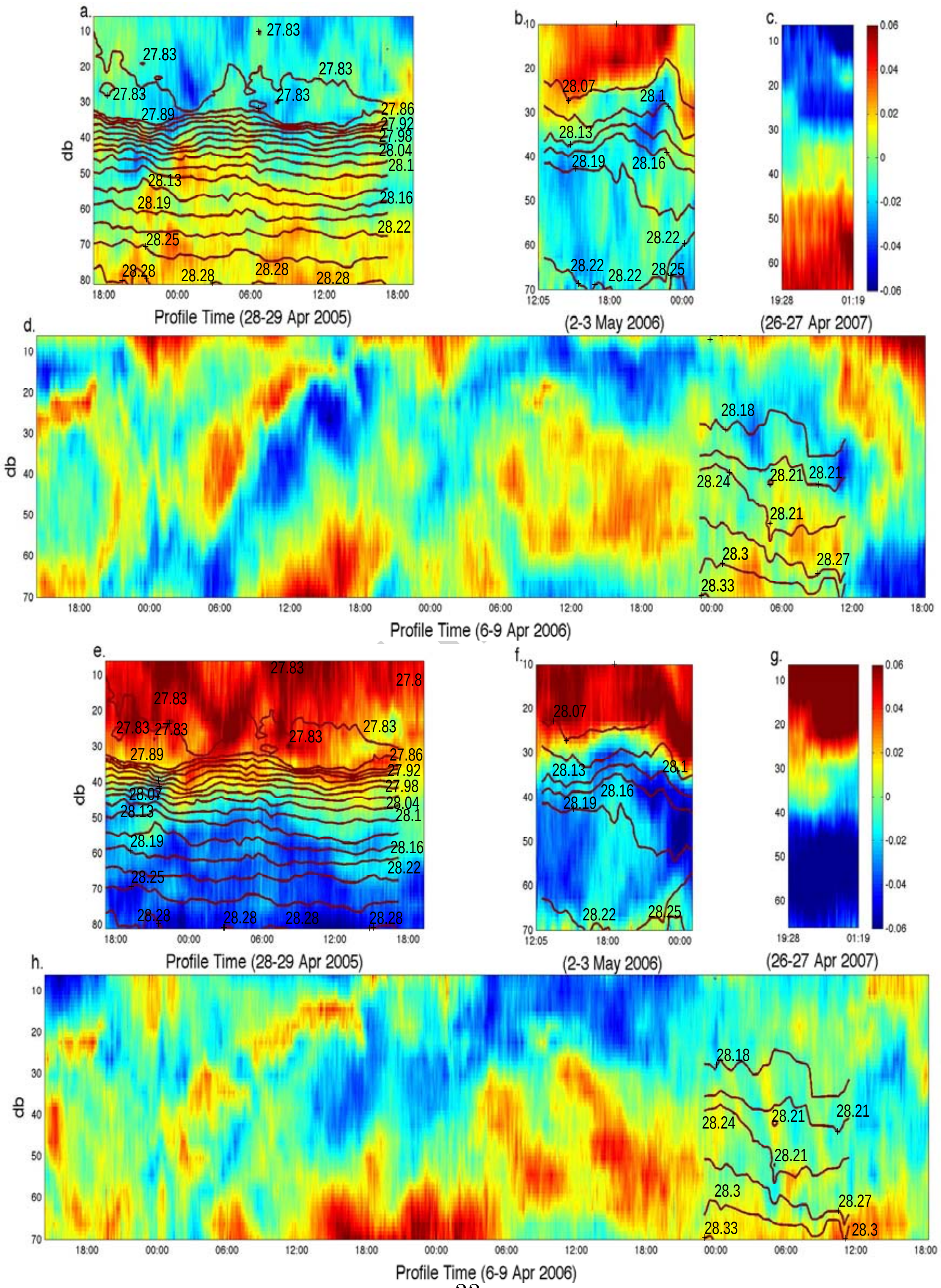

Figure 6: Zonal and meridional baroclinic velocities, $\mathbf{U}_{bc}$, in m/s for each time series. The top four figures represent the zonal component of $\mathbf{U}_{bc}$, and the bottom four display the meridional component for April 2005 (a & e), May 2006 (b & f), April 2007 (c & g), and April 2006 (d & h). Contours trace isopycnal surfaces.

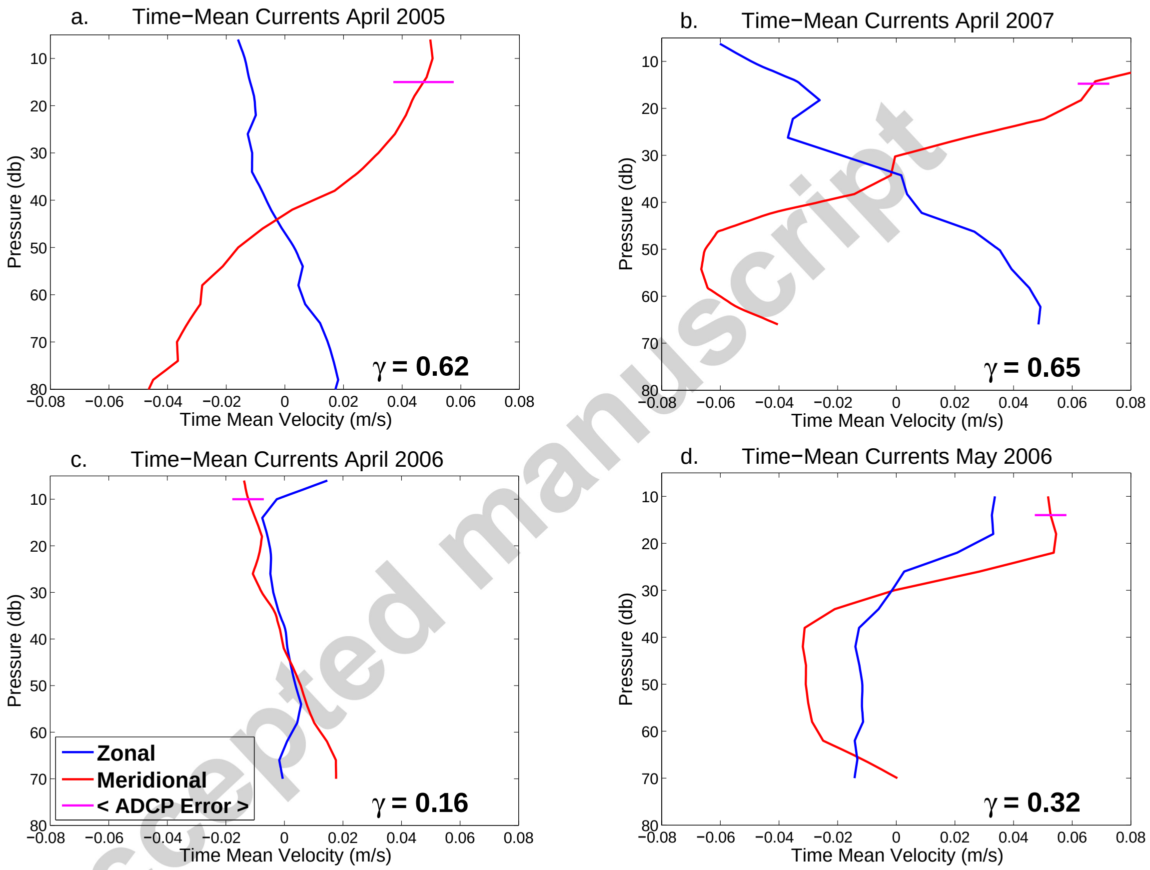

Figure 7: The time-mean of the zonal (blue) and meridional (red) components of the baroclinic velocity over a whole number of inertial periods (2 periods for April 2005 (a), 6 periods for April 2006 (c), and 1 period for May 2006 (d)) except for April 2007 (b) where the length of the time series is just under 6 hours (approximately $\frac{1}{2}$ an inertial period). The average time-mean ADCP error (magenta) is indicated for each time series.

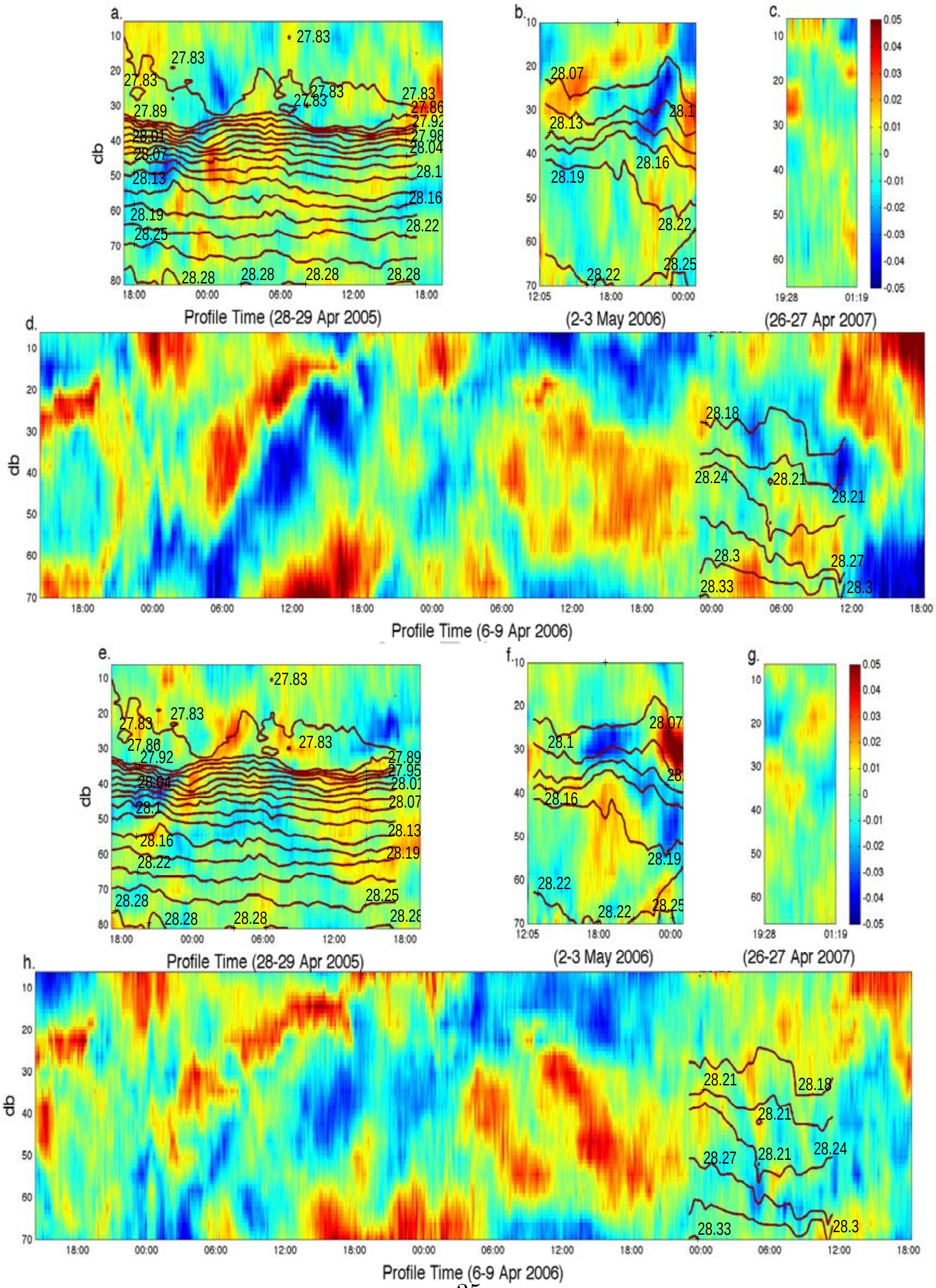

Figure 8: Zonal and meridional baroclinic perturbation velocities, $\mathbf{U}'_{bc}$ (baroclinic velocities, $\mathbf{U}_{bc}$, with the time-mean current (Figure 7) subtracted) in m/s. The top four figures represent zonal $\mathbf{U}'_{bc}$, and the bottom four are meridional $\mathbf{U}'_{bc}$ for April 2005 (a & e), May 2006 (b & f), April 2007 (c & g), and April 2006 (d & h). Contours trace isopycnal surfaces.

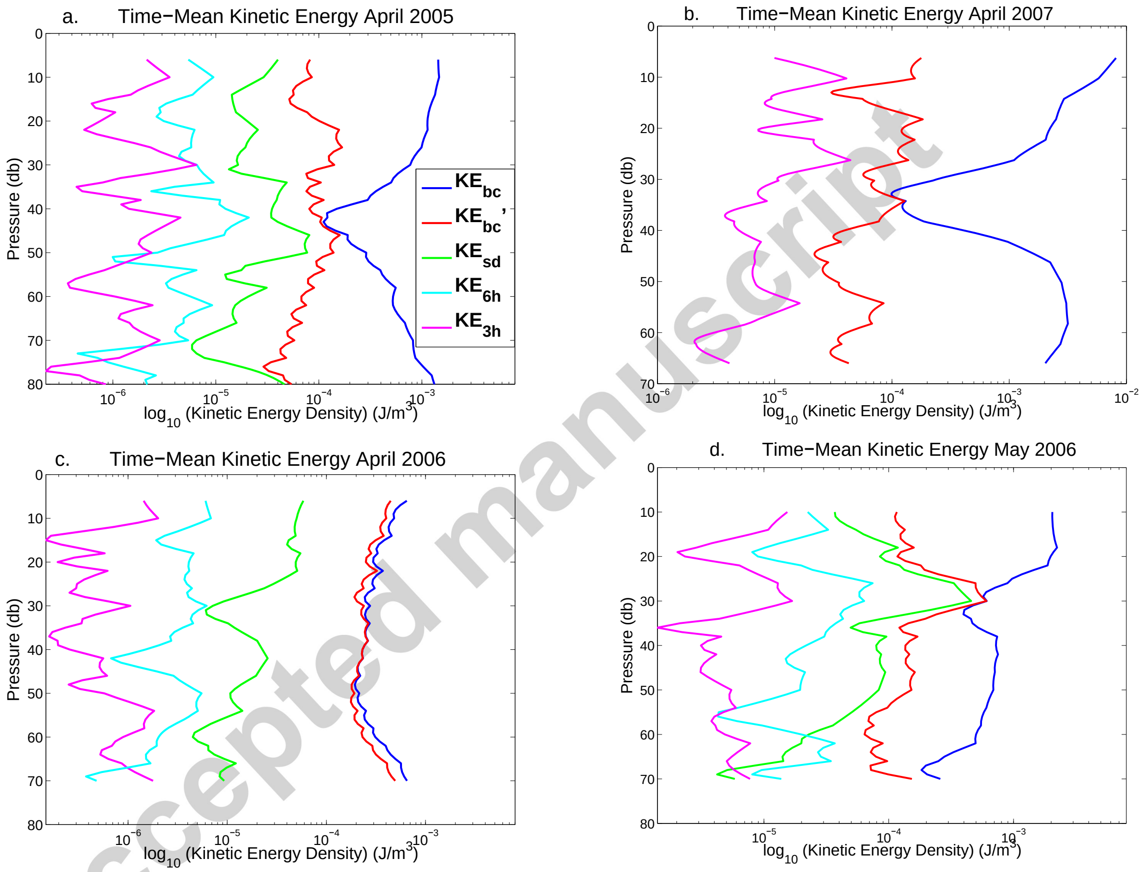

Figure 9: Time-mean kinetic energy of several components of the velocity field, including the baroclinic velocity ($\mathbf{U}_{bc}$), the baroclinic perturbation velocity ($\mathbf{U}'_{bc}$), the semidiurnal ($\mathbf{U}_{sd}$), the 6-hour ($\mathbf{U}_{6h}$), and the 3-hour ($\mathbf{U}_{3h}$) components for April 2005 (a), April 2007 (b), April 2006 (c), and May 2006 (d).

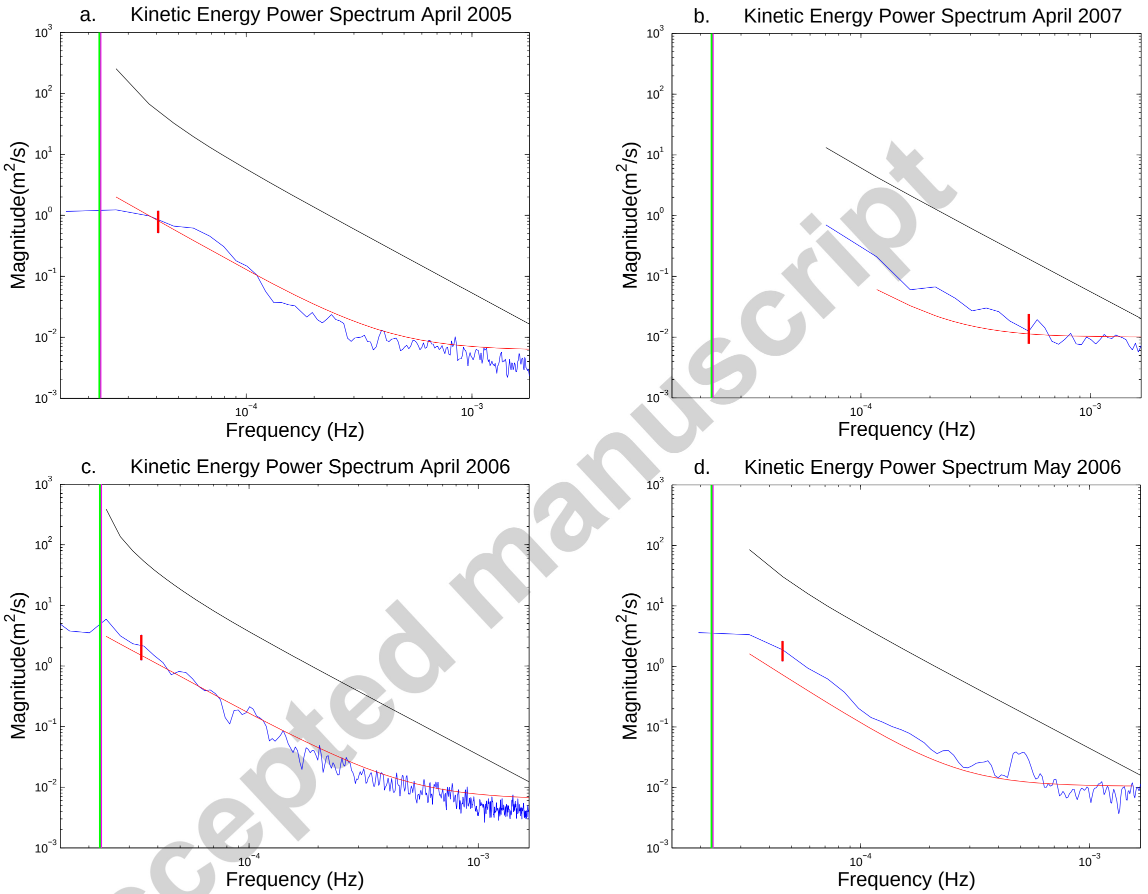

Figure 10: The observed kinetic energy power spectra, the sum of the square of the meridional power spectra and the square of the zonal power spectrum, (blue), and the power law fit to the spectra (red), together with the Garrett-Munk spectra (black) (Garrett & Munk, 1972, 1975) for April 2005 (a), April 2007 (b), April 2006 (c), and May 2006 (d). The nearly-collocated semidiurnal frequency (green) and inertial frequency (magenta) are the most energetic components of the power spectra. The red lines represent 95% confidence intervals.

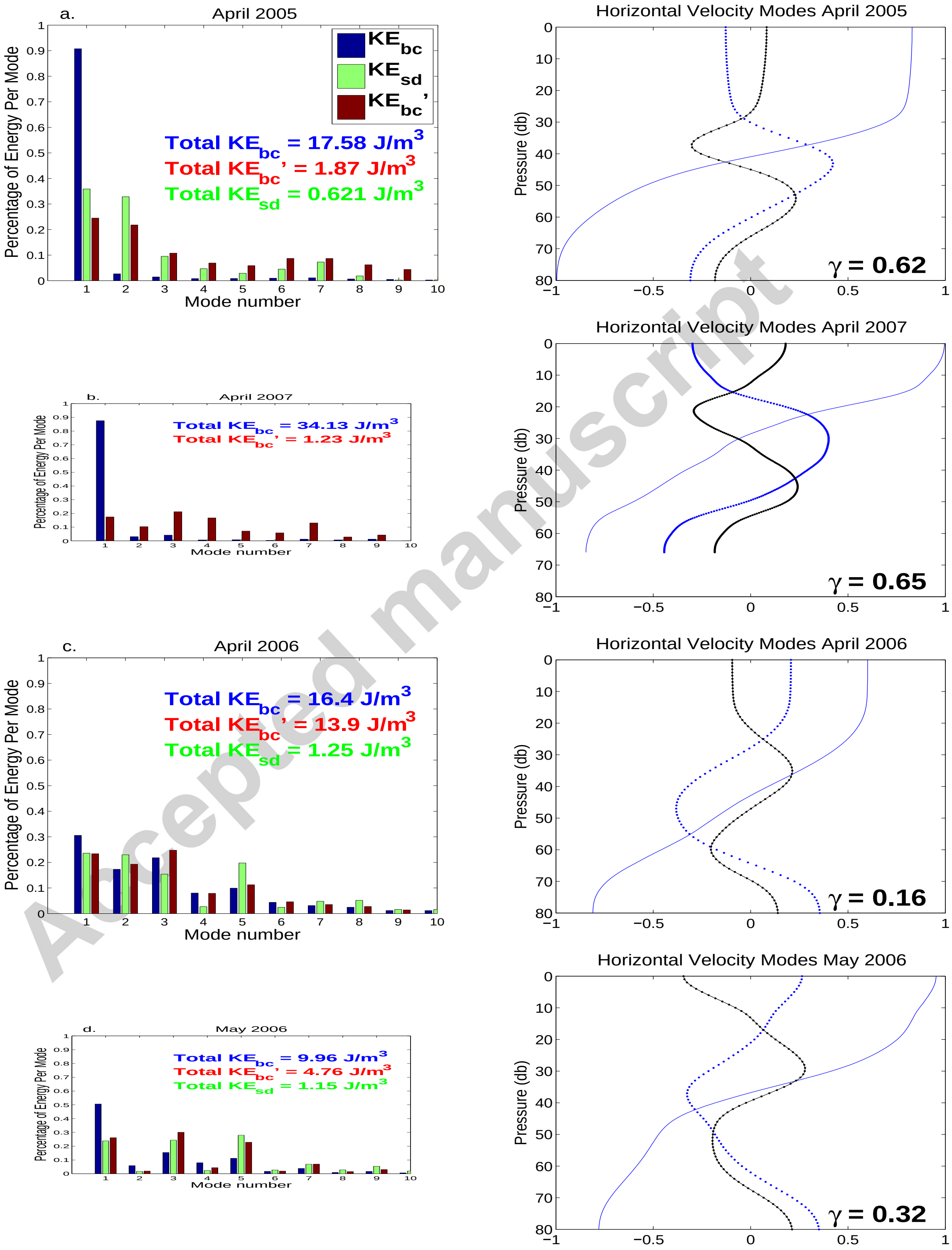

Figure 11: Percentage of kinetic energy in the first 10 modes of the total baroclinic velocity, KE_{bc}, baroclinic perturbation velocity, KE'_{bc}, and the semidiurnal velocity, KE_{sd}, (left), and the first 3 horizontal displacement modes (right) for April 2005 (a), April 2007 (b), April 2006 (c), and May 2006 (d).

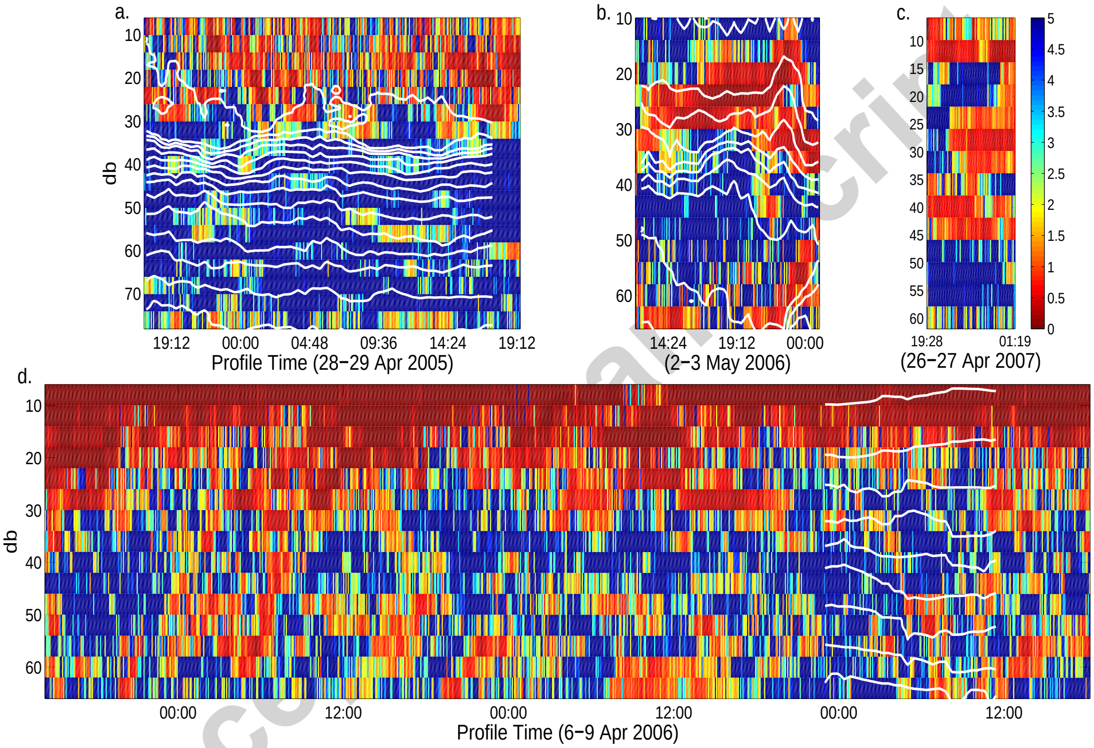

Figure 12: Richardson number ($Ri = N^2/S^2$), based on the average N^2 and the total shear squared ($S^2 = [(d\mathbf{u}/dz)^2 + (d\mathbf{v}/dz)^2]$) for April 2005 (a), May 2006 (b), April 2007 (c), and April 2006 (d). Contours trace isopycnal surfaces.

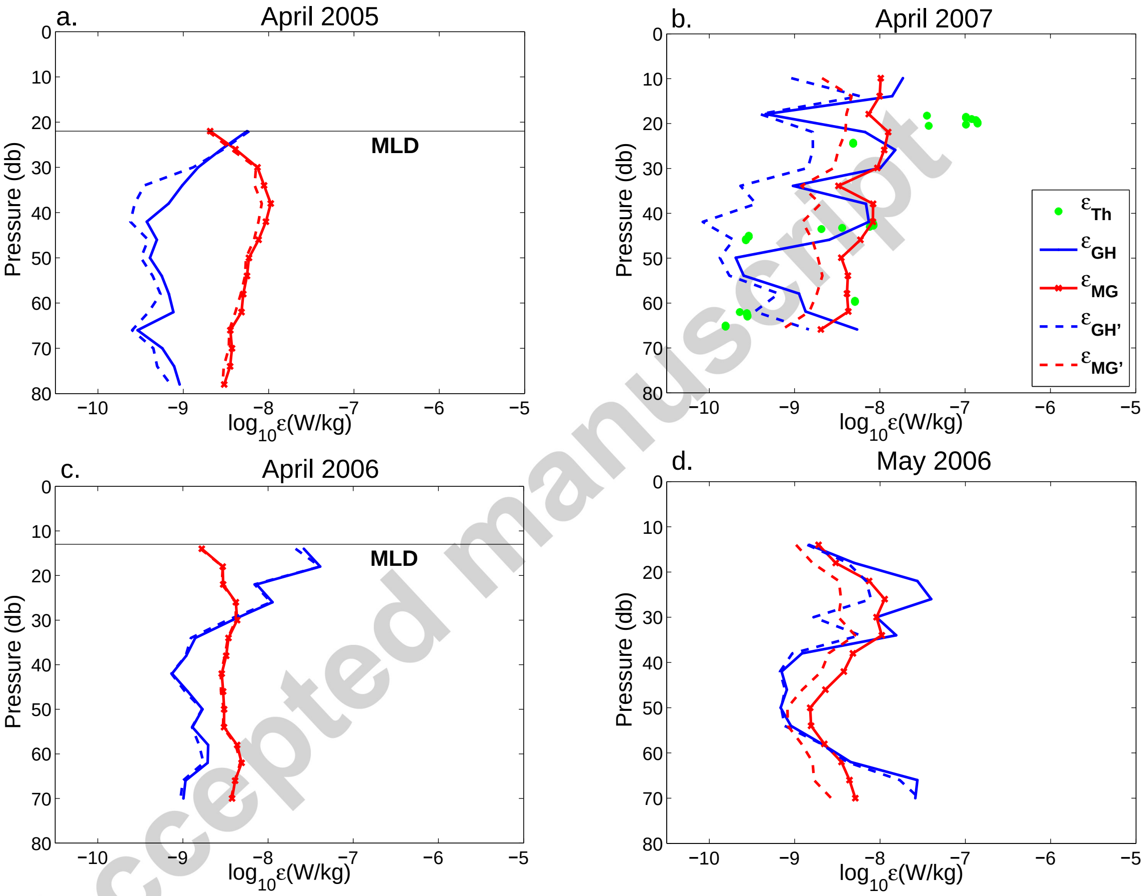

Figure 13: The time-mean dissipation rates, ϵ, based on Thorpe scale approximations, ϵ_{Th}, (green), Gregg-Henyey parameterization, ϵ_{GH}, (blue), and the MacKinnon-Gregg parameterization, ϵ_{MG}, (red). The mixed layer depth (MLD) is indicated by a black line for the two time series that exhibit a mixed layer, April 2005 (a) and April 2006 (c). Parameterizations were not calculated above this mixed layer depth.

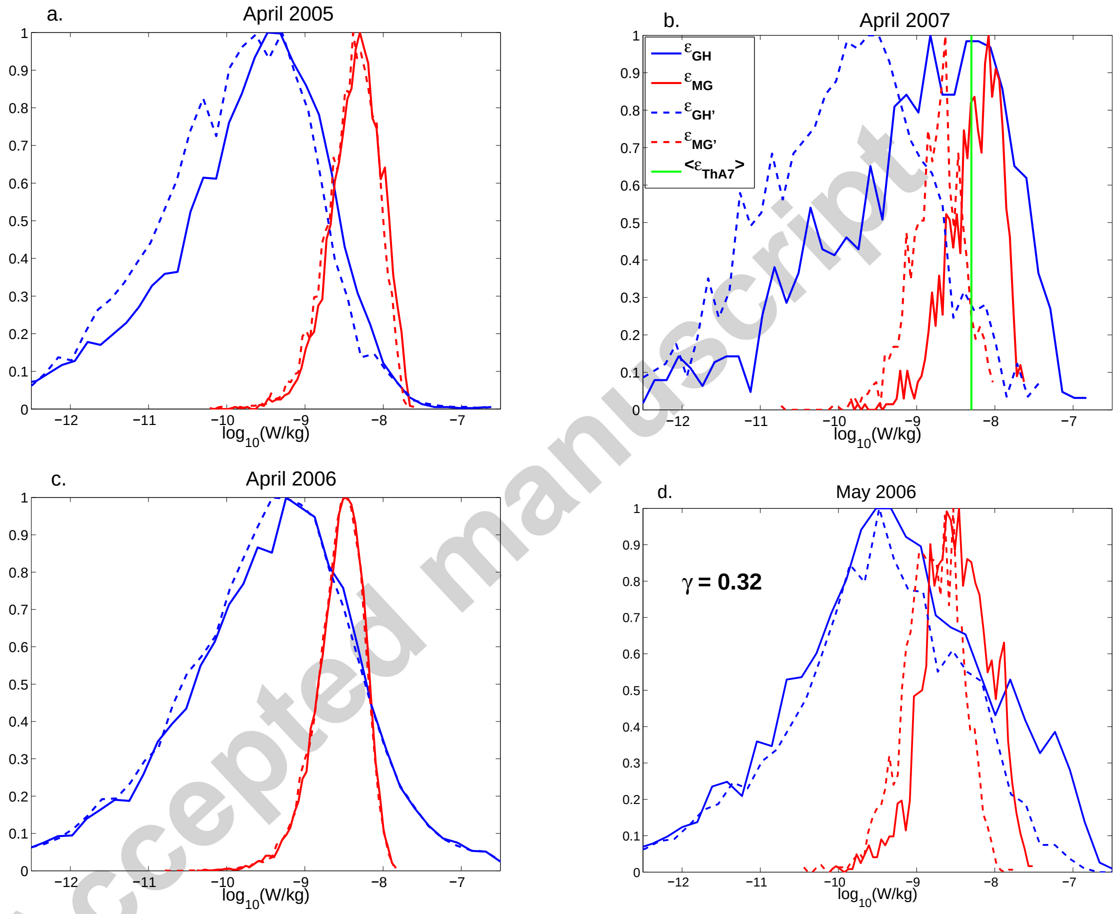

Figure 14: Probability Distribution Function of $log_{10}\epsilon$, based on Thorpe scale approximations, ϵ_{Th}, (green), Gregg-Henyey parameterization, ϵ_{GH}, (blue), and the MacKinnon-Gregg parameterization, ϵ_{MG}, (red), for April 2005 (a), April 2007 (b), April 2006 (c), and May 2006 (d). The ϵ derived from the baroclinic perturbation velocities, ϵ'_{GH} and ϵ'_{MG}, are indicated in dashed lines of the same color, respectively.

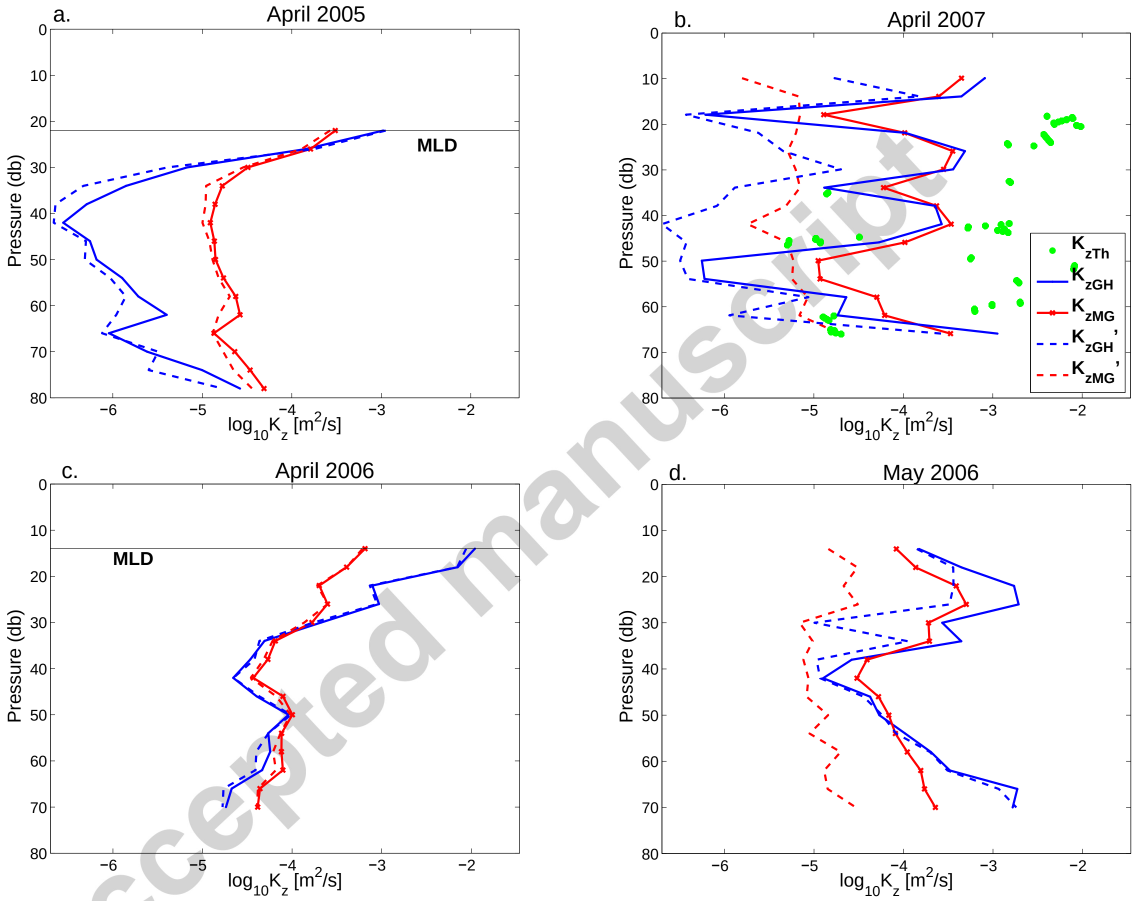

Figure 15: Average diapycnal diffusivities, κ_z, based on Thorpe scale approximations, ϵ_{Th}, (green), Gregg-Henyey parameterization, ϵ_{GH}, (blue), and the MacKinnon-Gregg parameterization, ϵ_{MG}, (red). The mixed layer depth (MLD) is indicated by a black line for the two time series that exhibit a mixed layer, April 2005 (a) and April 2006 (c). The κ_z derived from the baroclinic perturbation velocities, $\kappa_z{'}_{GH}$ and $\kappa_z{'}_{MG}$, are indicated in dashed lines of the same color, respectively.

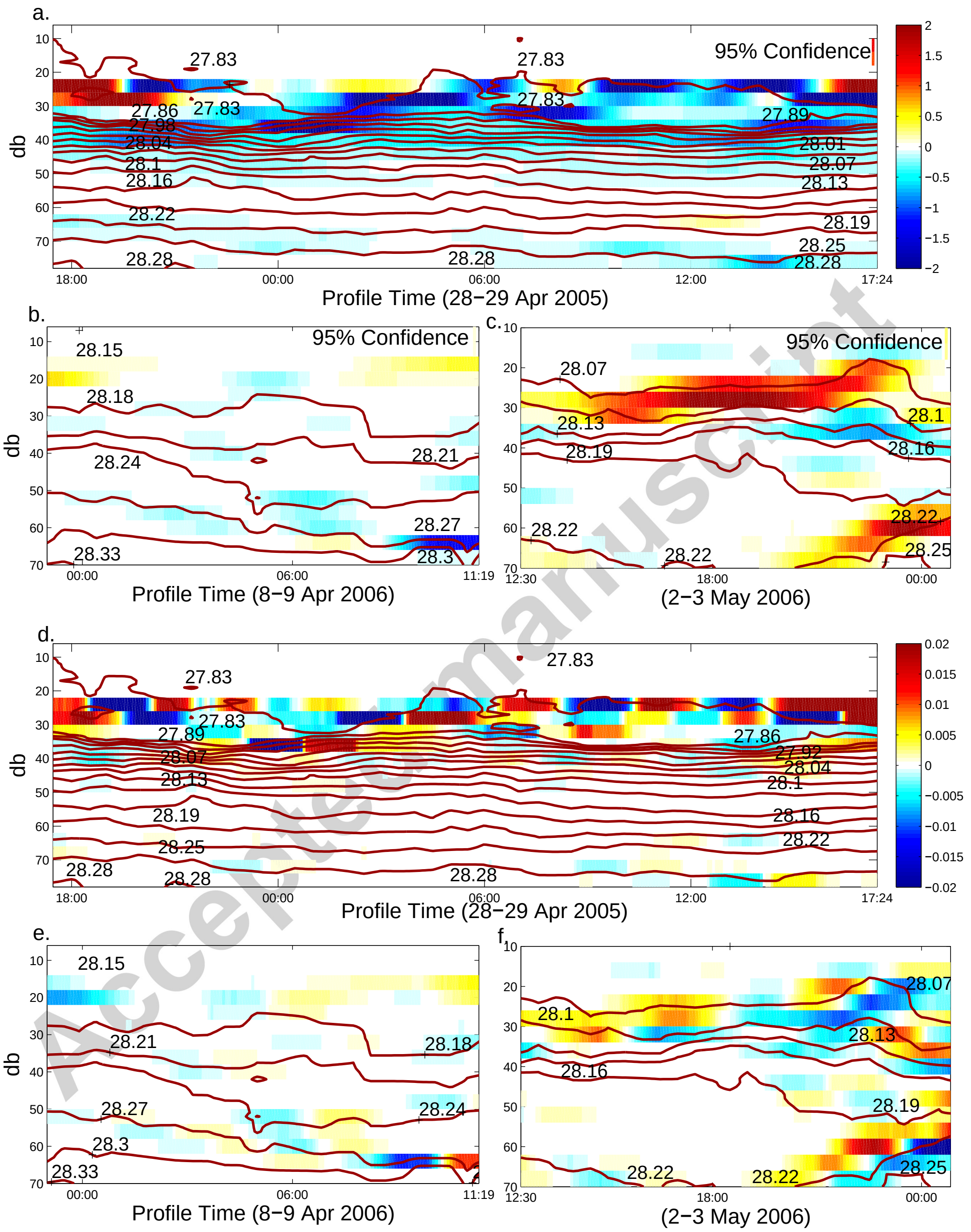

Figure 16: The heat flux, Q $[W/m^2]$ (top three plots), and the local heating/cooling rate, $\frac{dT}{dt}[^oK/month]$ (bottom three plots), determined from diapycnal diffusivities, κ_z, based on the MacKinnon-Gregg parameterization rate of turbulent dissipation, ϵ_{MG}, for the three time series with concurrent CTD and ADCP measurements: April 2005 (a & d), April 2006 (b & e), and May 2006 (c & f). Contours indicate isopycnal surfaces.